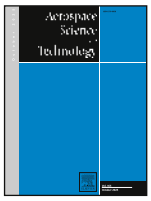
Aerospace Science and Technology 180 (2027) 113946



Contents lists available at ScienceDirect

Aerospace Science and Technology

journal homepage: www.elsevier.com/locate/aescte



Original article

Enhancing efficiency and stall margin in a transonic centrifugal compressor through modal-based diffuser vane design optimization

Ali Zamiri [a,b,*], Sam Lovett [b], Thomas C.S. Rendall [b], Minsuk Choi [c], Giovanna Barigozzi [a]

[a] Department of Engineering and Applied Sciences, University of Bergamo, Dalmine, Italy
[b] Department of Aerospace Engineering, University of Bristol, United Kingdom
[c] Division of Mechanical Systems Engineering, Myongji University, Yongin, Republic of Korea

ARTICLE INFO

Communicated by Dr Pooneh Aref

Keywords:
Centrifugal compressor
Vaned diffuser
Modal parametrization
Aerodynamic efficiency
Stall margin

ABSTRACT

Vaned diffusers are widely employed in centrifugal compressors to improve stage aerodynamic efficiency. However, their presence leads to a reduction in the stable operating range due to the increased tendency for flow separation within the diffuser passages. Consequently, identifying an optimal diffuser vane geometry is critical to achieve a compromise between aerodynamic performance and operational stability. In the present study, a three-dimensional compressible Reynolds-averaged Navier-Stokes (RANS) framework is adopted to investigate the effects of vane surface geometry modifications on the aerodynamic performance and stall margin of a centrifugal compressor. The baseline compressor is a transonic compressor with a relative inlet Mach number of 0.85 and a Reynolds number of approximately 1.5×10^6 at the design point. A novel modal shape parametrization technique was introduced to systematically modify the diffuser vane surface, providing a compact physics-informed representation of complex geometric variations. Fourteen design configurations were generated using an optimal space-filling (OSF) approach, based on two governing geometric parameters: mode number and mode amplitude. A surrogate model was constructed using a genetic aggregation algorithm (GA) technique trained with the numerical dataset, and a multi-objective genetic algorithm (MOGA) was then employed to identify optimal vane configurations that simultaneously enhance efficiency and extend stall margin. The results indicated that most of the modified designs enhanced both efficiency and operating range compared to the baseline case. These improvements are primarily attributed to the alteration of flow separation within the diffuser passage, a reduction in the incidence angle, and improved flow uniformity at the diffuser inlet. The optimal vane geometry exhibited a consistent aerodynamic performance improvement over the entire operating range, achieving an efficiency increase of approximately 4.1% at the design point, along with a 2.722% improvement in stall margin.

1. Introduction

Turbomachinery plays a critical role in modern engineering systems, supporting a wide range of energy conversion and thermal management technologies. Among these, centrifugal compressors have been widely utilized for more than a century in gas turbines, rotorcraft propulsion units, refrigeration cycles, and industrial process plants [1,2]. Their popularity is primarily attributed to their capability to achieve relatively high pressure ratios while maintaining a compact and mechanically robust configuration. In contrast to axial compressors, which typically require multiple stages to reach comparable performance, centrifugal compressors operate on a principle of dynamic compression through a high-speed rotating impeller. The increasing demand for advanced propulsion and energy systems has driven the need for centrifugal compressors with improved aerodynamic efficiency and enhanced operational reliability. Consequently, continuous advancements in compressor design methodologies, flow control strategy, and thermal management techniques have become essential to meet requirements in the turbomachinery industry.

An effective approach of enhancing the aerodynamic performance of centrifugal compressors is the implementation of vaned diffusers, which facilitate the conversion of the impeller's kinetic energy into static pressure through controlled flow deceleration [3,4]. In comparison with vaneless diffusers, vaned configurations generally provide higher pressure-recovery, particularly near the design operating point. However, the geometric constraints imposed by diffuser vanes can lead to significant flow non-uniformity within the diffuser passages. This non-uniformity behavior may narrow the stable operating range and increase

* Corresponding author at: Department of Engineering and Applied Sciences, University of Bergamo, Dalmine, Italy.
E-mail addresses: ali.zamiri@unibg.it (A. Zamiri), bv18812@bristol.ac.uk (S. Lovett), Thomas.Rendall@bristol.ac.uk (T.C.S. Rendall), mchoi@mju.ac.kr (M. Choi), giovanna.barigozzi@unibg.it (G. Barigozzi).

https://doi.org/10.1016/j.ast.2026.113946
Received 26 June 2026; Received in revised form 17 September 2026; Accepted 28 September 2026
Available online 1 October 2026
1270-9638/© 2026 The Author(s). Published by Elsevier Masson SAS. This is an open access article under the CC BY-NC-ND license (http://creativecommons.org/licenses/by-nc-nd/4.0/).

Nomenclature

A	Mode amplitude
C_p	Pressure recovery coefficient
d	Diameter of the diffuser vane leading edge
n	Mode number
P	Pressure
PS	Pressure side
SS	Suction side
TPR	Total pressure ratio
y^+	Normalized wall distance

Greek symbols

ζ	Diffuser pressure loss coefficient
η	Circumferential direction
ϕ	Normalized mass flow rate
ΔS	Entropy production
ΔSM	Stall margin improvement

Sub-, Superscripts

in	Inlet
out	Outlet
s	Static
t	Total

the sensitivity of the flow to incidence variations, thereby promoting the onset of flow instabilities inside the diffuser passages. These instabilities can trigger rotating stall or surge, leading not only to a reduction in aerodynamic efficiency but also, in severe cases, to structural damage within compressor stages [5,6]. Therefore, there is a strong need for design strategies capable of improving aerodynamic performance while simultaneously broadening the stable operating range of centrifugal compressors.

Various active and passive flow-control strategies have been proposed to reduce flow instabilities and extend the stable operating range of both centrifugal and axial compressors. Active flow control involves the deliberate addition of external energy into the flow field to modify and stabilize the internal aerodynamics. Typical approaches include modulated pulse jet vortex generator [7], plasma-based actuators, synthetic jet actuators [8], and adaptive tip-injection techniques [9]. Zhang et al. [8] proposed an adaptive jet flow-control system that couples stator-blade injection with rotor-tip injection in a transonic compressor. Their results demonstrated that, relative to the baseline configuration, the application of adaptive rotor-tip injection led to a noticeable improvement in both compressor efficiency and stall margin. In particular, the stall margin increased by as much as 7% when air injection was applied. Ak and Cadirci [9] numerically assessed the performance of a centrifugal compressor with a vaned diffuser using suction-based flow control under both design and near-stall operating conditions. Suction was applied through slots located at different circumferential positions and operated at various suction flow rates. Their findings indicated that the use of suction flow control resulted in improvements of approximately 0.85% in pressure ratio and 0.8% in efficiency compared with the baseline case. Skoch [10] experimentally investigated the effect of air injection into the vaneless region of a transonic centrifugal compressor to increase its operating range. A parametric study was conducted by varying the number of injectors, jet mass-flow rate, and injector location across different rotational speeds and tip clearances.

In contrast to active flow control methods, passive techniques do not require external energy input or additional devices. Instead, flow instability is enhanced through geometric modifications to the compressor stage. Common passive control approaches include grooves and riblets [11], blade slots, vortex generators, and different casing treatment concepts [12]. Zhao et al. [12] employed a dynamic mode decomposition framework to analyze the global transient behavior of a centrifugal compressor equipped with a self-circulating casing treatment and compared it with a baseline configuration. Their results demonstrated that, near the stall conditions, the casing treatment suppresses the interaction and propagation of upstream and downstream disturbances through an unsteady suction mechanism. As a result, the growth of tip leakage vortices is weakened, leading to improved flow stability near the impeller leading edge. Adjei et al. [13] proposed an arbitrary-shape volute optimization methodology to control circumferential pressure distortions over a wide operating range. A series of control points was distributed along the volute surface, and a design of experiment approach was adopted to explore the design space. The optimized volute geometry resulted in a 1.32% improvement in isentropic efficiency compared with the baseline case. The influence of blade squealer tips on the stall margin and aerodynamic efficiency of a transonic centrifugal compressor with a vaned diffuser was numerically investigated by Zamiri et al. [14]. Several squealer tip configurations with different cavity depths were examined for both main and splitter blades. The study revealed that an optimal cavity depth increased compressor efficiency and stall margin by approximately 0.32% and 1.02%, respectively, relative to the reference case. These improvements were mainly attributed to the reduction of tip leakage flow and circumferential velocity near the impeller shroud. Although a wide variety of passive flow control techniques have been proposed for centrifugal compressors, most of existing studies have primarily focused on modifications to impeller flow characteristics or inlet duct geometries.

In centrifugal compressors equipped with vaned diffusers, the interaction between the impeller and diffuser creates highly complex and unsteady flow characteristics near the diffuser throat, which are convected into the diffuser passages by the rotating impeller. In addition, due to the shape of the diffuser passages, the flow tends to be separated and fully turbulent. Previous investigations have shown that reduction of impeller/diffuser interaction and controlling separated flow within the diffuser passages [4,15,16] are key factors for improving both aerodynamic performance and compressor operating stability.

A limited number of experimental and numerical investigations have addressed the application of passive flow control techniques to compressor diffuser vanes. Zamiri et al. [17] proposed a two-dimensional cavity on the suction side of a diffuser vane to improve compressor performance. Three geometric parameters, cavity depth, distance from the vane leading edge, and cavity width, were considered as design variables. Using a genetic aggregation optimization scheme, they obtained an optimal configuration that improved aerodynamic efficiency by about 1% and increased the stall margin by 3.94% compared with the baseline design. Cui et al. [18] applied hub endwall contouring based on sinusoidal and Bezier curves with three geometric parameters, namely peak height, frequency coefficient, and peak radial position. Their results showed that the optimal endwall contouring extended the low mass flow operating range by up to 40% relative to the reference case. Zamiri et al. [19,20] also examined the effects of inclined leading edge diffuser vanes (ILEDVs) in a transonic compressor on the efficiency and stall margin improvement. An inclination angle of 30 degrees enhanced both design-point efficiency and stall margin by approximately 2.6% and 4%, respectively. Furthermore, the ILEDV configuration reduced the strength of the interaction between the impeller trailing edge and diffuser leading edge, resulting in lower pressure fluctuations and reduced aeroacoustic noise. Han et al. [21] studied the influence of vortex-induced losses in pipe diffusers with various design parameters for a high-pressure ratio centrifugal compressor. They demonstrated that decreasing the diffuser inlet-to-impeller exit radius ratio weakens hub-side vortices and reduces low-momentum flow regions near the hub, thereby improving diffuser performance. Zhang and Qi [22] investigated the impact of vane endwall clearances on centrifugal compressor efficiency. Although the endwall clearance reduced peak efficiency by about 2.7%, it increased the choke mass flow rate by nearly 20% at low rotational speeds compared with an ideal diffuser vane without clearance. Despite numerous experimental and numerical

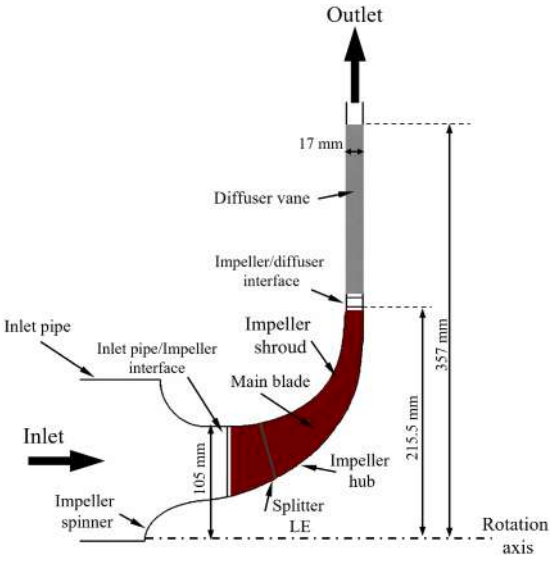


Fig. 1. Meridional view of the NASA CC3 centrifugal compressor.

studies reporting on diffuser vane optimization to enhance compressor stability and aerodynamic performance, most efforts have focused on modifying diffuser type or vane orientation angles, which may introduce trade-offs in aerodynamic efficiency and pressure ratio. To the best of the authors' knowledge, this work represents one of the first attempts to employ modal shape-parameterization techniques to the surface optimization of diffuser vanes. Compared with conventional parameterization methods reported in the literature [23–26], the proposed approach can reduce the number of design variables while preserving the capability to represent complex geometric variations, thereby improving the computational efficiency of the optimization process.

In this study, a coupled CFD-RANS and modal shape parameterization optimization framework is developed to improve the surface geometry of a centrifugal compressor diffuser vane with the aim of enhancing both efficiency and stall margin. Three-dimensional, steady, compressible RANS simulations are carried out using Simcenter STAR-CCM+ V2302 for a series of diffuser vane configurations in a transonic centrifugal compressor. The numerical results for the baseline geometry are validated with experimental data [27] over several operating conditions. The novel development of the present work is to assess the potential of the integrated RANS and subdivision modal shape parameterization approach for improving compressor aerodynamic performance and operating stability. Compressor design has been explored previously using problem-specific parameterizations (for example, using surface angles or characteristic dimensions such as thickness/chord), but the parameterizations here offers greater flexibility to explore spaces that the designer may not have originally envisaged. To this end, the diffuser vane surface is parametrized using two principal modal variables: the mode number (n) and the mode amplitude (A). Fourteen candidate geometries are generated using an optimal space-filling (OSF) design of experiment (DOE) method. A genetic aggregation optimization algorithm is employed to construct a surrogate model, and a multi-objective genetic algorithm (MOGA) is then used to determine the optimal vane configuration that simultaneously improves aerodynamic performance and stall margin. The proposed CFD-based modal shape optimization framework aims to improve the aerodynamic design process by integrating CFD with modal shape methodology and to provide a systematic approach that can be applied to advanced turbomachinery optimization.

2. Compressor and modified diffuser configuration

In the present numerical investigation, the NASA CC3 transonic centrifugal compressor, previously tested in the Small Engine Components test rig at NASA Glenn Research Center [27], is adopted as the baseline configuration. The compressor consists of an unshrouded impeller followed by a vaned diffuser. The impeller consists of 15 main blades and 15 splitter blades, whereas the downstream diffuser includes 24 two-dimensional wedge-shape vanes. Fig. 1 presents the meridional flow path of the compressor. At the design operating point, the impeller rotational speed is 21,789 rpm, delivering a total pressure ratio of 4:1 and a mass flow rate of 4.56 kg/s. The splitter blades are located at the mid-pitch of main blade passages in the circumferential direction, with their leading edges positioned at 30% of the main blade chord. The impeller has a non-uniform tip clearance, increasing from 0.154 mm at the leading edge to 0.203 mm at the trailing edge. The diffuser vane leading edges are located at a radius corresponding to 108% of the impeller exit radius. The vanes extend axially with a passage height equal to that at the impeller exit and are designed with a 7.8 ° divergence angle. A summary of the principle geometric parameters and operating specifications of the compressor is provided in Table 1, while further details regarding the compressor configuration and experimental setup can be found in [27,28].

Numerical simulations were performed on a centrifugal compressor equipped with a baseline diffuser vane and a modified diffuser vane configuration developed through a modal shape parameterization technique. The computational domain, shown in Fig. 2, consists of three primary regions: a stationary inlet pipe, a rotating impeller, and a station-

Table 1
Geometric parameters and operating conditions of the compressor stage.

Operating conditions	
Total pressure ratio	4:1
Design mass flow rate	4.56 kg/s
Impeller	
Rotational speed	21,789 rpm
Number of blades	15 Main + 15 Splitter
Inlet tip diameter	210 mm
Inlet blade height	64 mm
Impeller exit diameter	431 mm
Exit blade height	17 mm
Backsweep angle	50 °
Tip clearance at leading edge	0.154 mm
Tip clearance at trailing edge	0.203 mm
Diffuser	
Number of vanes	24
Vane leading edge radius	1.08 of the impeller exit radius
Vane height	17 mm
Divergence angle	7.8 °
Diffuser exit diameter	714 mm

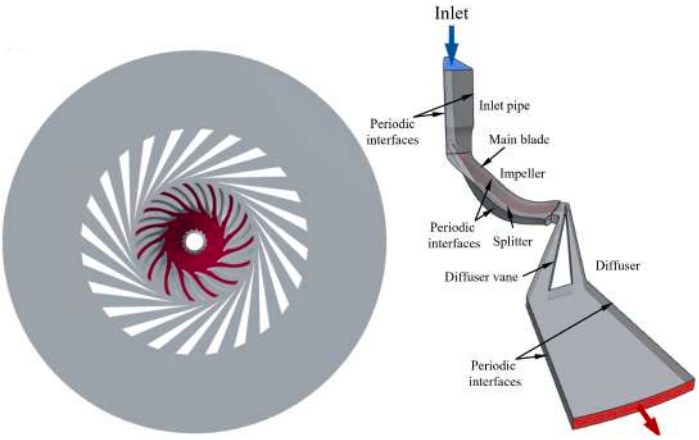


Fig. 2. Computational domain of the centrifugal compressor. Left: full-annulus view of the compressor stage showing the impeller and diffuser. Right: single-passage computational model employed for numerical simulations.

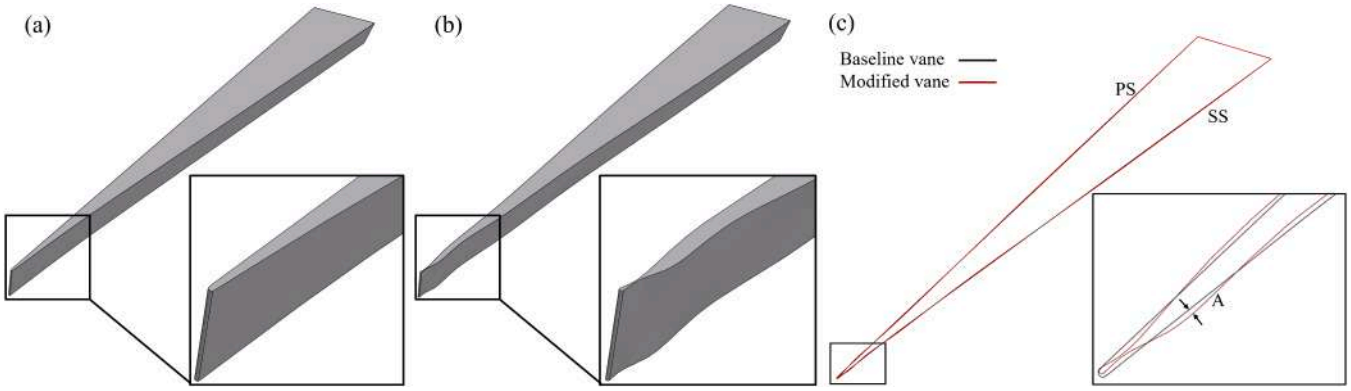


Fig. 3. (a) Baseline wedge-type diffuser vane, (b) modified diffuser vane obtained using modal shape parameterization technique (generated using mode number 12 and a normalized mode amplitude of 1.88), (c) comparison of diffuser vane profiles on the mid-span plane for the baseline case and modified case using the modal shape parameterization method.

ary diffuser. Fig. 2 provides both a full-annulus view of the compressor stage and the single-passage computational model adopted for the numerical simulations. Fig. 3(a) and (b) present the conventional wedge diffuser vane and the corresponding modified diffuser vane geometry (generated using mode number 12 and a normalized mode amplitude of 1.88), respectively. It should be noted that the modal parameterization was applied directly on the three-dimensional vane surfaces. As illustrated in Fig. 3(c), two geometric parameters, the mode number (n) and the mode amplitude (A), are introduced as design variables to investigate the effect of diffuser vane surface shape variations on aerodynamic performance and stall margin. It is important to note that the modal deformation is applied exclusively to the diffuser vane, while the impeller geometry, including both the main and splitter blades, remained unchanged throughout the study to isolate the effects of the vane modifications.

3. Numerical method

3.1. Computational grid and boundary conditions

A single-passage configuration was utilized to reduce computational cost while enabling increased mesh density within the impeller and diffuser passages. The resulting grids at representative locations in both impeller and diffuser sections are shown in Fig. 4. The computational grid, generated using Simcenter STAR-CCM+ V2302 software, consists of approximately 2,500,000 control volumes. A polyhedral topology was employed in combination with 21 prism layers near all solid boundaries. This approach is well suited to highly curved and twisted blade geometries, as it improves discretization accuracy through enhanced face connectivity and more isotropic cell quality. As indicated in Fig. 4, local mesh refinement was applied near the leading edges of the impeller and diffuser blades to better resolve strong curvature, stagnation regions, and associated flow gradients. Furthermore, to adequately capture near-wall effects, the first layer height of wall-normal grid spacing was approximately $2\mu m$ to control the non-dimensional wall distance (y^+) below 2 over the diffuser vane surfaces (Fig. 4), satisfying the requirement of the SST (shear stress transport) turbulence closure. It should be noted that the overall meshing strategy and grid resolution follow guidelines established in the authors' previous investigations [4,17,19,20].

Periodic boundary conditions are applied using a rotational periodic transformation interface about the compressor axis. The impeller rotation is modeled using a rotating reference frame at a constant rotational speed of 21,789 rpm. The coupling between the rotating and stationary domains is treated using a mixing-plane interface model, which circumferentially averages flow variables across the interface [29]. Air as an ideal gas with a total pressure and total temperature of 1 atm and 288 K, respectively, was set at the inlet. At the outlet, a mass flow rate boundary condition is imposed at the design operating point, whereas a static pressure boundary condition is applied for off-design conditions, including near-surge and choke regimes. All solid walls are defined as adiabatic and no-slip boundary conditions. The impeller shroud is specified with a counter-rotating wall condition to account for the relative motion between the rotating impeller and the stationary casing.

3.2. Solver setup

The three-dimensional, steady, compressible RANS equations were solved using Simcenter STAR-CCM+ V2302. The $k-\omega$ SST turbulence model formulation was selected as the turbulence model, which is widely adopted for turbomachinery applications due to its robustness in predicting adverse pressure gradients, flow separations, and complex secondary flows in rotating blade passages [29,30]. A coupled algebraic multigrid (AMG) solver with a second-order spatial discretization scheme was used for the diffusive terms of the governing equations [31]. At the design point, convergence was assumed when the normalized residuals of all governing equations fell below 10^{-5}. For off-design conditions, convergence was assessed based on established criteria [17,32,33], requiring that variations in mass flow rate and total-to-total efficiency remained within 0.001 kg/s and 0.3%, respectively, over 500 iterations. As described in Section 3.1, the compressor performance map, ranging from choke to near-stall conditions, was obtained by progressively increasing the outlet static pressure in small increments of 600 Pa. This procedure ensured stable convergence at each operating point with accurately capturing the performance curve. All simulations were performed on the University of Bristol high-performance computing cluster utilizing 64 processing cores, with approximately 30 h required to obtain the complete compressor characteristic from choke to surge for each case.

3.3. Numerical validation

A grid-independence study was conducted to quantify the effect of mesh resolution on the predicted aerodynamic performance of the centrifugal compressor. Three meshes were generated for the baseline configuration, comprising approximately 1,200,000, 2,500,000, and 4,700,000 cells. Fig. 5 presents the total pressure ratio and total-to-total isentropic efficiency obtained from the RANS simulations for the three grid resolutions, along with available experimental data [27] at the design operating point. As the number of cells is increased from 2,500,000 to 4,700,000 cells, only marginal variations are observed in both performance parameters. Considering the negligible improvement in accuracy beyond 2,500,000 cells, alongside the associated increase in computational cost, the intermediate mesh (2,500,000 cells) was selected for all subsequent simulations in this study.

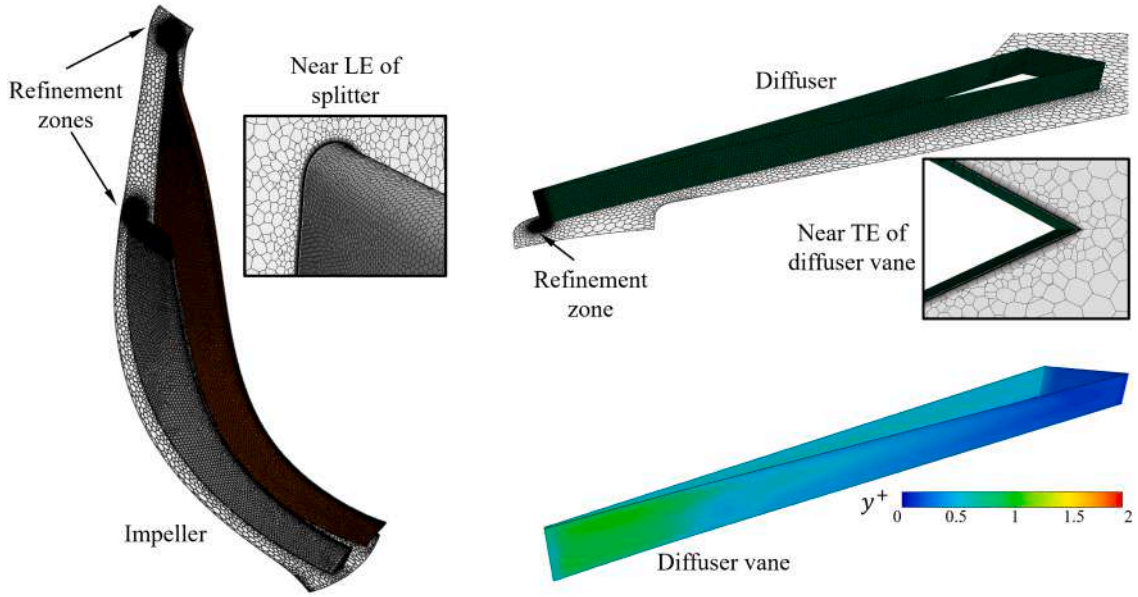


Fig. 4. Computational mesh distribution at representative sections of the impeller and diffuser passages, along with the y^+ distribution on the diffuser vane surfaces.

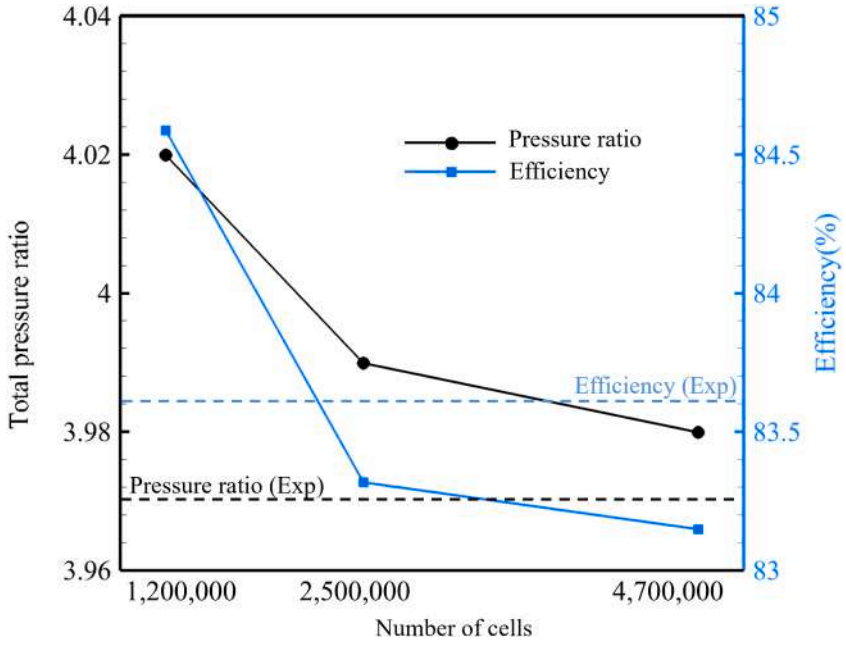


Fig. 5. Grid independence test for the baseline centrifugal compressor at the design operating point.

To assess the reliability of the numerical method, the baseline compressor performance map predicted by the numerical simulations is compared with the corresponding experimental measurement [27], as shown in Fig. 6. It is observed that the present computational framework accurately reproduces the overall trends of the compressor characteristics, demonstrating good agreement with the experimental data over a wide range of operating conditions, from choke to near-surge.

4. Optimization method

The pressure recovery of vaned diffusers is strongly dependent on the internal flow structures within the passages, with particular sensitivity to the onset and extent of flow separation. In transonic centrifugal compressors, wedge-type diffuser vanes are widely used due to their robust aerodynamic performance under compressible, shock-dominated flow conditions. The diffuser design is characterized by multiple geometric parameters, including the leading edge shape, vane camber and blade angle, thickness distribution, and radial as well as meridional displacement. However, optimizing of these parameters through computational and experimental studies remains challenging because of the high dimensionality of the design space. Therefore, an efficient shape parameterization method is required to represent the geometry using a reduced set of design variables while preserving the essential aerodynamic features.

In this study, a multi-objective optimization framework was implemented according to the following procedure: 1) a baseline compressor configuration was selected, 2) the design variables and objective functions were selected, 3) the bounds of the design variables were determined through a preliminary CFD-based sensitivity analysis, 4) a design of experiment approach was used to generate a representative set of

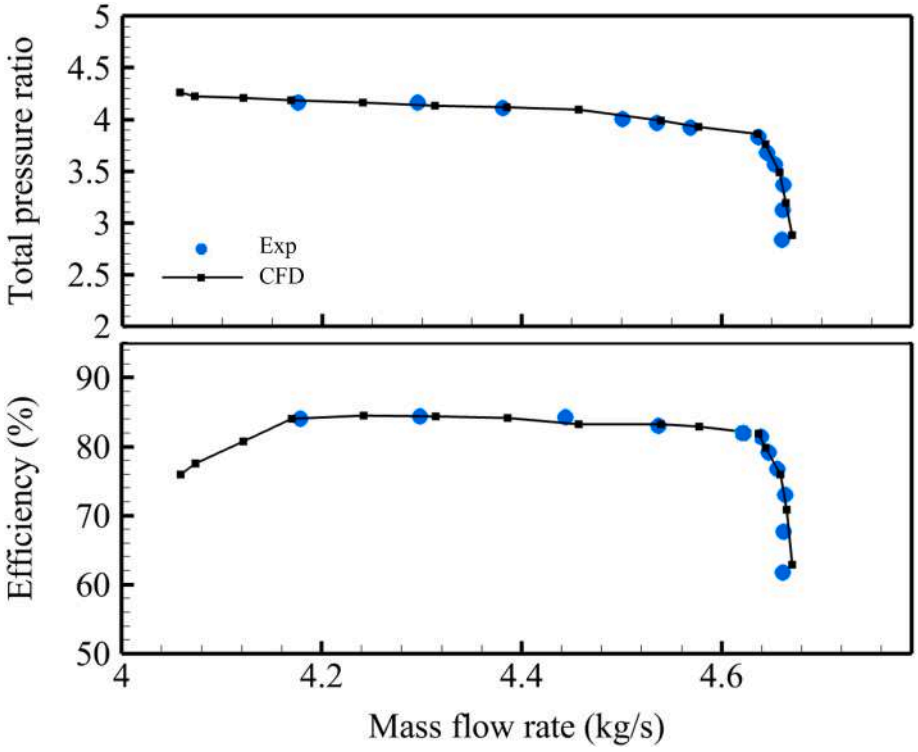


Fig. 6. Comparison of compressor map characteristics between experimental measurements [27] and CFD simulations for the baseline compressor configuration.

sampling points, 5) a surrogate model was constructed using the CFD-generated database, 6) the optimal geometric parameters were identified by maximizing the selected objective functions. Finally, the optimization process was stopped once the optimal point was obtained.

4.1. Modal subdivision shape parameterization

Optimization requires being able to convert from the vector of design variables to the shapes to be explored by the optimizer. Flexibility and efficiency are both desired, so that as many possible geometries may be explored without an excessive number of design variables, which would otherwise increase the dimensionality of the design space unreasonably and leave the optimizer with a harder challenge.

Within the context of diffusers, many different configurations have been explored [34], but an optimal parameterization is not clear. This is in contrast to, for example, aerofoil or wing optimization where parameterizations are readily available and their capabilities documented on established aerofoil libraries [35]. Bespoke diffuser parameterizations may be considered, using ranges of radii, angles, thicknesses and lengths, for example as applied to centrifugal pumps [36], but these limit the design space available to the optimization and constrain results to what practitioners perceive might be beneficial, rather than leaving this open to the optimization to determine.

To resolve this challenge within this work, a modal parameterization is employed around subdivision surfaces. However, rather than employing subdivision control points directly [37], a set of design vectors is derived through a singular value decomposition of the subdivision limit matrix for an initial surface mesh [38,39]. These design vectors can then be summed with the coordinate positions of the initial surface mesh to arrive at the query geometry for each step of the optimization. Each vector applies global, wave-like deformations to the surface of different frequencies. Subdivision is a mesh smoothing and refinement algorithm, which defines a limit surface from a coarse surface mesh through a process of recursive refinement [40,41]. The process works on the basis of inserting additional surface nodes between existing nodes in the surface mesh, before a smoothing operation is applied over all nodes.

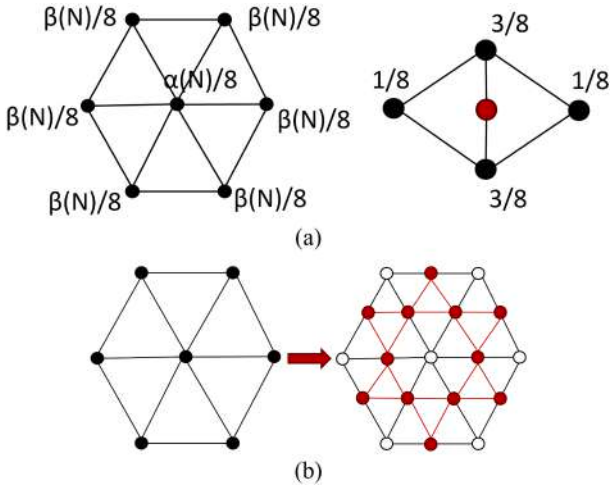


Fig. 7. (a) The stencils used to determine positions of existing and new vertices. (b) The neighborhood of a vertex of valence 6 shown before and after one subdivision refinement.

In more detail, for the control point Loop subdivision scheme (from which the modal approach is derived) as in Fig. 7, every vertex (the initial 'control points') is replaced by a weighted average of its surrounding vertices. The values for $\alpha(N)$ and $\beta(N)$ this stage of the process are found using

$$\alpha(N) = \frac{3}{8} + \left(\frac{3}{8} + \frac{1}{4}\cos\frac{2\pi}{N}\right)^2 \tag{1}$$

and

$$\beta(N) = (1 - \alpha_N)/N \tag{2}$$

where N is the valence of the central vertex. Following this, as shown in Fig. 7, *new* vertices are inserted at edge mid-points, before these new points are connected to make new faces.

This process is applied recursively, so that generating the $n+1$ level from level n may be written, with $\mathbf{C}$ the coordinate vector of the surface points, as

$$\mathbf{C}_{n+1} = \mathbf{A}\mathbf{C}_n \tag{3}$$

and this operation may be nested, with a sequence of (growing) $\mathbf{A}$ matrices multiplied to give a matrix that maps from any one level through many refinements to a final desired level. However, it is also possible to apply a limit argument and determine a *single* matrix that will take any vector of input points and map them to their final positions, were the refinement process to be repeated an infinite number of times.

The limit positions of each of the surface mesh vertices are still calculated as a weighted average of their starting coordinates and those of the surrounding vertices [42]. This allows a single matrix multiplication to be written which maps each point on the initial surface to its limit position

$$\mathbf{C}_\infty = \mathbf{L}\mathbf{C}_0 \tag{4}$$

where $\mathbf{C}_0$ gives the initial coordinates of the surface mesh and $\mathbf{C}_\infty$ gives the coordinates of the limit position of the same points. The limit matrix, $\mathbf{L}$, is a sparse smoothing matrix, which contains adjacency information (in similar form to the original $\mathbf{A}$ matrices, but with modified weights that take account of the limit behavior). The limit matrix is suitable for singular value decomposition, and therefore the subdivision control points themselves are not used directly here; rather, the connectivity information present in the subdivision scheme is used for construction of the orthogonal space via these modes.

The singular value decomposition of this sparse matrix may be written as

$$\mathbf{L} = \mathbf{U}\mathbf{S}\mathbf{V}^* \tag{5}$$

where $\mathbf{U}$ is a matrix whose columns are an orthogonal basis in the column space of $\mathbf{L}$; $\mathbf{S}$ is a diagonal matrix of singular values; and $\mathbf{V}^*$ is the conjugate transpose of $\mathbf{V}$, a matrix whose columns are an orthogonal basis in the row space of $\mathbf{L}$. The columns of $\mathbf{U}$ can be used as a set of orthogonal design vectors of increasing frequency which can be scaled with an amplitude and summed with the surface mesh coordinates to apply smooth deformations. These design vectors can be defined as the modes. For reference, mode numbers can be given to the successive columns.

To reduce the dimensionality to align with the low numbers of design variables that were used, the deformations were kept constant across the height of the diffuser vane upper and lower surfaces. Modes were computed for the two-dimensional projection of the geometry, which could then be extrapolated over the height of the vane. The upper and lower surfaces were allowed to deform without geometric constraints. Due to the variation in mesh density across the vane, the deformations at the leading edge of the vane were of higher spatial frequency. It was expected that this variation would be beneficial, as the objective was found to be more sensitive to geometric changes at the leading edge.

An important question in using a modal decomposition to reduce the dimensionality of the design space is how much of the higher dimensional space can still be accessed by the optimization. Reducing dimensionality benefits the numerical process, but there is inevitably a corresponding reduction in available design space. Using the modal subdivision method and for a library of over 1000 aerofoils, geometric reconstruction to within a standard wind tunnel geometric tolerance has been explored by Lovett et al. [38], with results indicating that using 20 modes allows over 90% of the library to be reconstructed within tolerance, as defined by Kulfan [43]. This of course does not imply the same for vane geometries, which differ from aerofoils and for which no test library easily exists. Nonetheless, the implication is that for single-digit numbers of modes, the optimal result is unlikely to be within the Kulfan tolerance of the true optimum. Despite this, the results of Lovett et al. [38] also indicate that for the NACA0012 test optimization, optimization results do not improve greatly after 20 modes are used, and importantly, the majority of the performance improvement is accessed by the first few modes. The implications for the compressor work here are (i) the optimal shape will not be within Kulfan tolerance of the true optimum, and (ii) that despite this, useful improvements are available with only single-digit numbers of design modes. This tradeoff is necessary to avoid the cost of running RANS optimizations in a high-dimensional design space. It is likely, but not guaranteed, that (based on the data in [38]) further performance improvements on the order of 10s of % might be achievable if it were possible to use 10–20 modes. Therefore, no explicit modal truncation criterion is used in this work; rather, within the tight constraints on the number of modes that may be employed in this work, a manual choice is the most pragmatic route.

Table 2
Specifications of design variables.

Design variables	Lower bound	Upper bound
Mode number (n)	1	14
Mode amplitude (A)	$-2.25\ d$	$2.25\ d$

Fig. 8 shows the first six modes significantly amplified for illustrative purposes in the chord normal direction for the vane geometry. Note that actual displacement sizes used are also dependent on the modal amplitudes chosen, so real displacements used in computations are smaller than shown here, and any apparent crossover in this figure would not take place unless amplitudes were set too high. It is convenient to order the modes in terms of an ascending mode number, which usually corresponds to increasing spatial frequency (note that this may or may not correspond to the output ordering from the numerical computation), and therefore gives an indication of the number of maxima/minima along the surface. Within the set of early frequency modes, it is not straightforward to determine which may offer the greatest performance improvement, so this question must be answered through the optimization. Also, although high frequency deformations in isolation are unlikely to offer aerodynamic improvements, the smooth shapes formed through constructive or destructive summations of those higher spatial frequencies may still offer benefits and ideally should remain included. As Fig. 8 illustrates, the early modes correspond to increasing spatial frequencies of symmetric/asymmetric thickness and camber.

In summary, using a design of experiment approach necessitates a small number of design variables. Geometrically orthogonal modes permit this to be effective by giving an efficient coverage of spatial deformations, and the matrix system that a subdivision surface scheme produces is highly amenable to this type of decomposition. Even after a compact decomposition of this type, it is still necessary to select those modal deformations anticipated to provide the greatest benefits, with the lowest frequency shapes likely being the most attractive for this purpose.

4.2. Design variables and objective functions

As shown in Fig. 3, two key geometric parameters of the diffuser vane surface, the mode number and mode amplitude, are selected as design variables within the optimization framework. It should be noted that the mode amplitude is normalized by the diffuser vane leading edge diameter (d). The primary aim of the present study is to enhance the aerodynamic performance of the centrifugal compressor through systematic modifications of the diffuser vane surface geometry. In particular, the optimization seeks to simultaneously increase the total-to-total isentropic efficiency at the design operating condition and extend the stable operating range, quantified in terms of the stall margin. Accordingly, these two performance metrics are defined as objective functions and are maximized during the optimization process. The lower and upper bounds of the design variables are listed in Table 2, which were carefully selected following preliminary geometric assessment of the deformed diffuser vane surfaces. These bounds restrict the accessible design space that produces physically feasible configurations. Although the modal parameterization allows the pressure and suction surfaces to deform freely, increasing the modal order or modal amplitude beyond

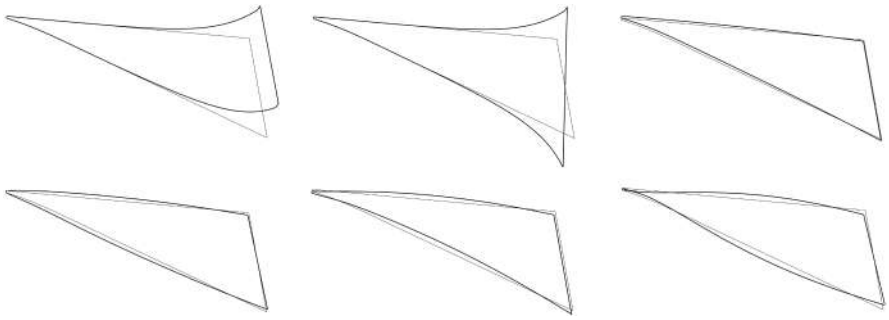


Fig. 8. Plots of the first six design variable deformations summed with the original coordinates of the vane. The geometry has been rotated by 45° anticlockwise and scaled 3× in the new rotated y direction for visualization purposes.

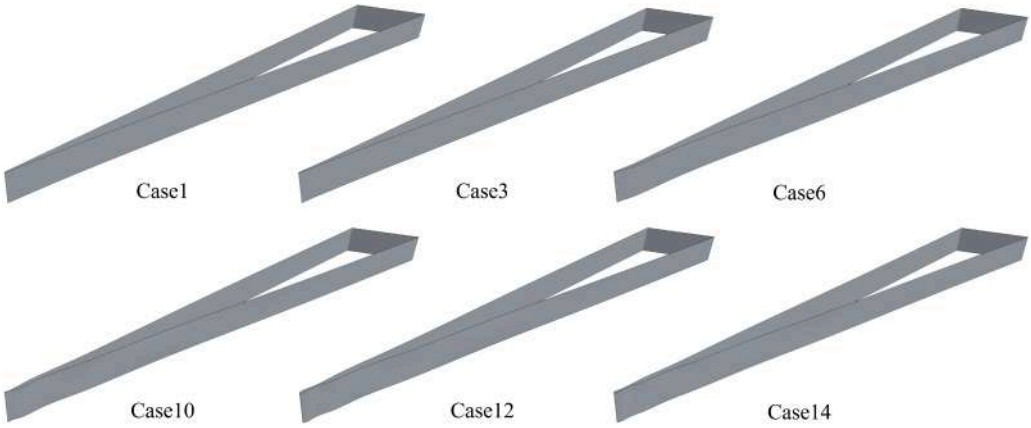


Fig. 9. Schematic illustration of selected diffuser vane configurations modified via modal shape parameterization.

Table 3
Specifications of the various design cases by the DoE approach.

Case Number	Mode Number (n)	Mode Amplitude (A/d)
1	1	0.18
2	2	1.54
3	3	−1.88
4	4	−0.52
5	5	0.86
6	6	2.25
7	7	−1.54
8	8	−0.18
9	9	1.20
10	10	−2.25
11	11	−0.86
12	12	1.88
13	13	0.52
14	14	−1.20

the selected limits results in intersections between the pressure and suction surfaces, particularly near the leading edge of the diffuser vane, where larger modal amplitudes and higher spatial frequency deformations were found to produce geometric interference. Consequently, geometric feasibility in the present optimization is therefore controlled primarily through a priori restriction of the modal design space rather than through an explicit surface-intersection constraint evaluated at every optimization iteration. The modal basis was limited to the first 14 modes, which provides sufficient geometric flexibility while maintaining physically realistic and manufacturable diffuser geometries.

4.3. Design of experiment

The objective of the DOE approach is to identify a minimal representative set of sampling points that enables the accurate construction of a response surface. In the current study, an optimal space-filling (OSF) DOE approach was employed to efficiently explore the design space [44]. The OSF approach is based on Latin Hypercube sampling (LHS). It is first generated as a standard LHS design and then refined through an iterative optimization process. During this refinement, the fundamental properties of LHS are preserved (no overlap of samples within rows or columns), while the spatial distribution of points is improved by maximizing the distance between samples. As a result, the OSF design provides a more uniform coverage of the design space, allowing the key design trends to be captured with a limited number of simulations. In this work, fourteen design configurations were generated using the OSF method and evaluated by the CFD approach, as summarized in Table 3. Fig. 9 illustrates selected representative geometries in comparison with the baseline diffuser vane. The modified configurations exhibit distinct geometric deviations, particularly a wavy deformation near the leading edge, which arises from the applied modal shape parameterization technique.

4.4. Genetic aggregation response surface methodology

After completing the numerical simulations for all configurations generated through the DOE, a response surface methodology (RSM) was used to establish a statistical relationship between the design variables and the objective functions. To construct the surrogate model, a genetic aggregation (GA) technique was adopted [45]. This approach belongs to the class of ensemble meta-modeling methods, in which multiple surrogate models are combined to improve predictive performance. The GA-based framework automatically selects and combines candidate meta-models by using a genetic algorithm. In this process, a population of surrogate models is generated and evaluated simultaneously using GA approach with a specified maximum relative error tolerance of 1%. To satisfy this accuracy criterion, the GA algorithm generates five additional

refinement points, while these points are then used to cross-validate the predictive accuracy of the response surface. The fitness function of each meta-model is assessed based on both its prediction accuracy at the sample points and its overall robustness. The coefficient of determination (R^2) of the final GA response surface is 0.988, indicating good predictive performance. The resulting ensemble response surface is then expressed as a weighted average of the individual surrogate predictions:

$$\hat{y}_{ens}(x) = \sum_{j=1}^{N_M} W_j . \hat{y}_j(x) \tag{6}$$

where $\hat{y}_{ens}(x)$ denotes the ensemble prediction, y_j is the prediction of the jth surrogate model, N_M represents the total number of meta-models, and W_j ($W_j = \sum_{j=1}^{N_M} W_j = 1$ and $W_j \geq 0$) is the corresponding weight factor. The optimal weighting coefficients are determined by minimizing the root mean square error (RSME) of the ensemble prediction evaluated at the DOE sample points:

$$RSME(\hat{y}_{ens}) = \sqrt{\frac{1}{N_M} \sum_{j=1}^{N_M} \left(y(x_j) - \hat{y}_{ens}(x_j)\right)^2} \tag{7}$$

where x_j denotes the jth design point, and $y(x_j)$ is the corresponding output parameter.

After constructing the surrogate model, a multi-objective genetic algorithm (MOGA) [46–49] was employed to determine the optimal diffuser surface configuration. The adopted approach is based on a hybrid implementation of the well-established NSGA-II (non-dominated sorted genetic algorithm-II), combined with a controlled elitism strategy to enhance convergence while maintaining diversity along the Pareto front. This model is capable of handling a wide range of design variables and constraints, making it well suited for complex aerodynamic optimization problems. In the present study, an initial population of 1000 samples was generated, and the maximum number of iterations was set to 20. The optimization converged after 549 evaluations. Convergence was achieved when the convergence stability percentage reached 1.52, with the maximum allowable Pareto percentage set to 70%, at which point the optimization process was terminated.

5. Numerical results

5.1. Effects of diffuser vane configuration on compressor efficiency and stall margin

Fig. 10 compares the total pressure ratio and total-to-total isentropic efficiency of the centrifugal compressor for the baseline diffuser and three modified vane configurations generated using the modal shape technique. The corresponding experimental data for the baseline case are also included in Fig. 10. The cases highlighted in Fig. 10 are defined as follows: Case11, which provides the highest isentropic efficiency at the design point; Case9, which exhibits the lowest isentropic efficiency at the design point together with the smallest stall margin; and Case5, which achieves the largest stall margin. The results indicate that variations in the diffuser vane surface geometry have a pronounced impact on both the aerodynamic performance, particularly at the design condition, and the operating range of the compressor. Case11 shows a considerable improvement in isentropic efficiency not only at the design point but also across a wide range of operating conditions. In contrast, Case9 exhibits degraded aerodynamic performance relative to the baseline configuration, accompanied by the lowest stall margin among the investigated cases.

Fig. 11(a) and (b) show the normalized pressure ratio and efficiency, respectively, for all designed configurations relative to the baseline diffuser at the design operating point. The results indicate that variations in the diffuser vane surface geometry significantly influence both the pressure ratio and performance. Overall, most of the proposed designs exhibit improvements in pressure ratio and efficiency compared with the reference configuration. Among the tested cases, Case3 achieves the largest increase in pressure ratio, with an enhancement of approximately 11% relative to the baseline. In terms of efficiency, Case11 demonstrates the best performance, showing an improvement of about 3.1%.

Fig. 12 shows the variation in stall margin improvement (ΔSM) compared to the reference case for all designed diffuser vane geometries. The stall margin is used as a quantitative indicator of compressor stability and operating range, reflecting the sensitivity of the flow field to modifications of the diffuser surface geometry, and is defined as [50]:

$$\Delta SM(\%) = [(1 - \frac{TPR_{peak}}{TPR_{stall}} \times \frac{\dot{m}_{stall}}{\dot{m}_{peak}})_{test} - (1 - \frac{TPR_{peak}}{TPR_{stall}} \times \frac{\dot{m}_{stall}}{\dot{m}_{peak}})_{Ref.}] \tag{8}$$

where $\dot{m}_{peak}$ and $\dot{m}_{stall}$ denote the mass flow rates at the design point and stall, respectively, while TPR_{peak} and TPR_{stall} represent the corresponding total pressure ratio. As presented in Fig. 12, only a limited number of configurations lead to a reduction in stall margin, whereas most of the proposed designs exhibit a noticeable improvement in stall margin compared to the baseline compressor. Among all investigated cases, Case5 (characterized by a mode number of 5 and an amplitude of -0.52d) achieves the largest enhancement, with an increase in stall margin of approximately 2.52%. A combined assessment of Figs. 10–12 further indicates that the influence of diffuser vane surface geometry on compressor performance and stall margin is strongly dependent on the specific vane configuration.

5.2. Effects of diffuser vane configuration on the impeller flow field

Before examining the flow structures within the diffuser passage, it is essential to evaluate how modifications to the diffuser vane surfaces affect the upstream flow field inside the impeller passages. Fig. 13(a) and (b) compare the mid-span pressure distributions within the impeller for Case5 (corresponding to the maximum stall margin) and Case9 (corresponding to the minimum stall margin), respectively. As expected, the pressure progressively increases from the impeller inlet to the outlet due to centrifugal and rotational effects. A detailed comparison indicates that both the magnitude and spatial distribution of pressure within the impeller passages remain nearly identical for the two configurations. This observation shows that the geometric modifications applied to the diffuser vanes have a negligible effect on the upstream flow field inside the impeller. Such behavior is consistent with the characteristics of transonic centrifugal compressors, where a shock-induced wake typically forms near the diffuser throat and blocks the upstream propagation of flow disturbances originating from the diffuser passages. A similar trend was reported in previous studies on cavity optimization of diffuser vanes [17], in which the upstream impeller flow remained unaffected by downstream geometric alterations.

5.3. Effects of diffuser vane configuration on flow characteristics within the diffuser passages at design point

One of the primary factors governing compressor performance and stability is the development of low-momentum and separated flow regions within the diffuser passages. Fig. 14 illustrates the velocity magnitude contours at the mid-span cutting plane of the diffuser passages for the baseline and all modified diffuser configurations. As observed in Fig. 14, low-velocity regions, represented by the dark blue contours, appear inside the diffuser passages in all cases, indicating different levels of flow separation. For the baseline diffuser vane, flow separation originates near the leading edge of the diffuser vane on the suction side and progressively extends downstream toward the trailing edge. This behavior is mainly associated with the adverse pressure gradient and the impeller/diffuser interaction. For the modified geometries, although the

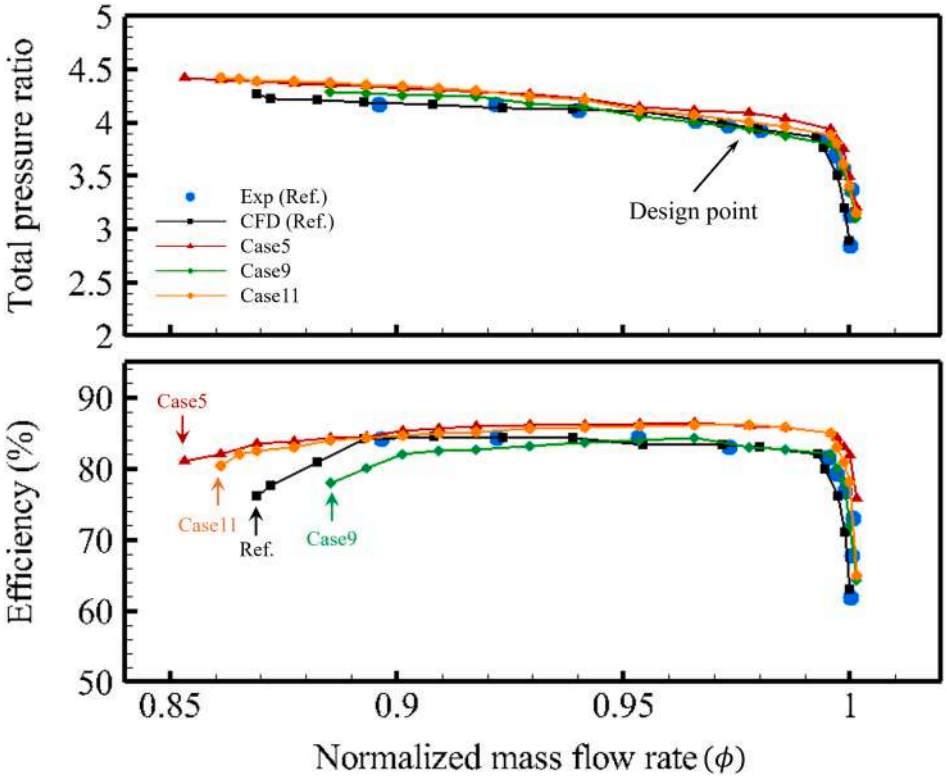


Fig. 10. Centrifugal compressor performance map for the baseline and three modified vane configurations.

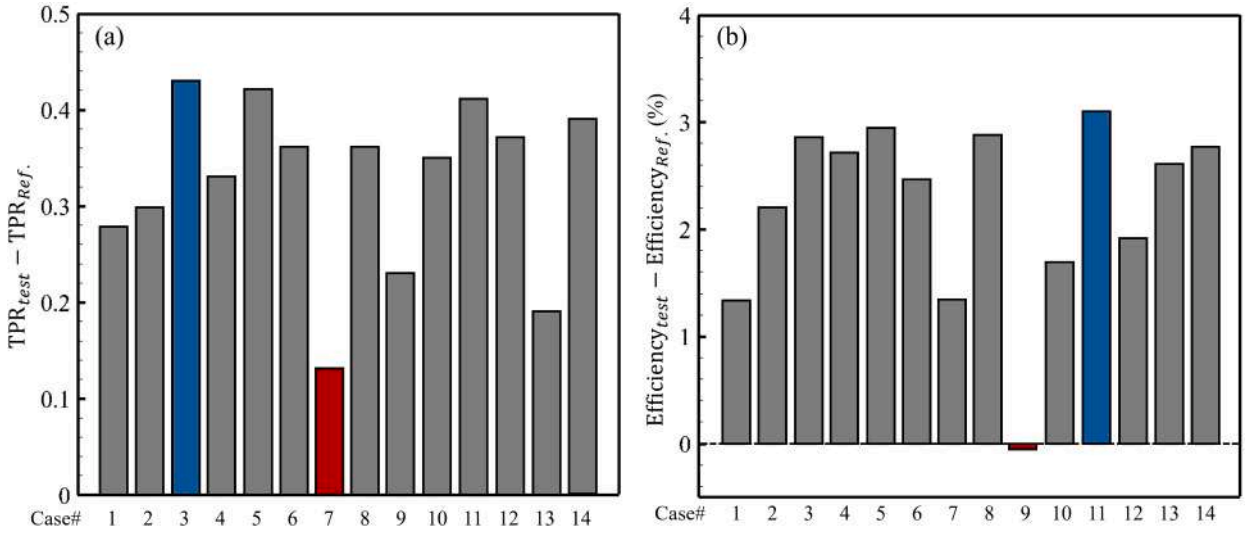


Fig. 11. Comparison of aerodynamic performance between the designed configurations and the baseline case: (a) total pressure ratio gain, (b) total-to-total efficiency.

extent of the low-momentum region is generally reduced, its spatial distribution varies depending on the vane shape. In several cases, the separation zone shifts between the suction and pressure sides, reflecting the sensitivity of the internal flow structure to variations in leading edge position and vane camber. Case5, corresponding to the maximum improvement in stall margin, exhibits a markedly smaller separated region that is displaced downstream toward the diffuser exit. In addition, the velocity distribution at the diffuser throat becomes more uniform compared with the baseline case, suggesting improved flow guidance and reduced blockage. In contrast, Case1, Case2, and Case9, which are associated with negative stall margin values, exhibit extensive low-momentum regions occupying a significant portion of the diffuser passage. In these configurations, the separation zone tends to shift toward the pressure side, which can be attributed to the upstream shift of the leading edge and the resulting obstruction of the incoming impeller discharge flow. Furthermore, Case10 demonstrates the formation of a localized high-velocity region immediately downstream of the leading edge on the pressure side, as indicated in Fig. 14. This feature is indicative of local flow acceleration and potential shock formation, which may introduce additional aerodynamic losses and flow unsteadiness inside the diffuser passage. Overall, the results confirm that modifications to the diffuser vane geometry, particularly changes in leading edge geometry and surface curvature, strongly influence the internal flow structure and the aerodynamic performance of the compressor.

To evaluate how modifications to the diffuser vane geometry influence the internal pressure field, normalized static pressure contours at

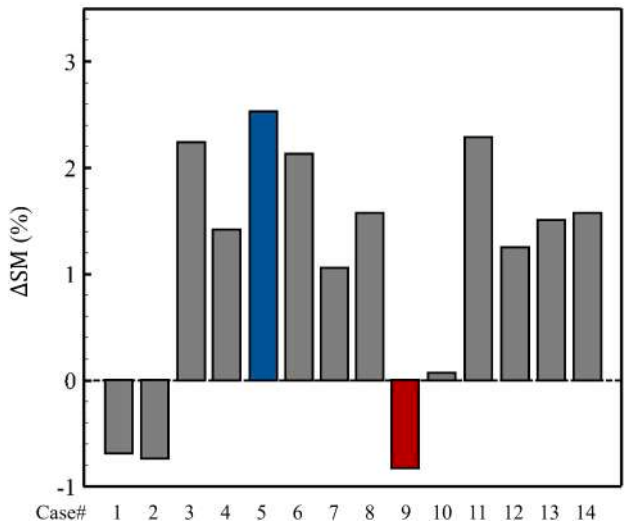


Fig. 12. Comparison of stall margin improvement for all designed cases.

the mid-span plane of the diffuser passages are compared for the reference and designed vanes in Fig. 15. The selected designs represent distinct aerodynamic characteristics: Case3 exhibits the highest total pressure ratio, Case5 provides the best stall margin, Case9 corresponds to the worst stall margin and efficiency, and Case11 delivers the best efficiency. For most designed configurations, the pressure magnitude inside the diffuser passage increases relative to the reference case, with the exception of Case9. Among all cases, Case3 shows the most pronounced pressure rise. A notable difference is observed in the stagnation pressure distribution near the diffuser leading edge, which varies significantly between the cases. In the reference case, a large and nearly symmetric stagnation region forms around the leading edge. This high-pressure zone redirects the incoming flow toward the circumferential direction and reduces the effective diffuser throat area, thereby promoting the development of flow separation on the pressure side immediately downstream of the leading edge. Application of the modal shape technique alters both the leading edge geometry and its position, leading to substantial changes in the stagnation pressure distribution. In Case9, the leading edge is displaced toward the suction side surface, and the resulting curvature downstream of the leading edge induces a strong recirculation region and an extended low-pressure zone. As a result, flow separation develops along the entire suction side surface, consistent with the flow structure previously identified in Fig. 14. In contrast, the other designed cases exhibit a smaller stagnation pressure region compared to the baseline configuration, with the stagnation point displaced toward the pressure side. This redistribution contributes to a more favorable flow structure within the diffuser passage.

To evaluate the impact of diffuser vane surface modifications on flow separations and associated aerodynamic loss mechanisms within the diffuser passages, the pressure recovery coefficient and total pressure loss coefficient were computed for all designed configurations relative to the baseline case, as presented in Fig. 16(a) and (b), respectively. The pressure recovery coefficient (C_p) and total pressure loss coefficient (ζ) are defined as:

$$C_P = \frac{P_{t,out} - P_{s,in}}{P_{t,in} - P_{s,in}} \tag{9}$$

$$\zeta = \frac{P_{t,in} - P_{t,out}}{P_{t,in} - P_{s,in}} \tag{10}$$

where P_t and P_s denote the total and static pressures, respectively, and the subscripts *in* and *out* refer to the inlet and outlet of the diffuser passage.

As illustrated in Fig. 16(a), most modified configurations demonstrate an improvement in pressure recovery compared to the reference diffuser, following a trend consistent with overall compressor performance enhancement reported in Fig. 11. However, Case7 and Case9 deviate from this general behavior, corresponding respectively to the lowest total pressure ratio and the smallest efficiency improvement. Among all cases, Case3 (highlighted in blue) exhibits the most significant enhancement, with an increase of approximately 9% in pressure recovery relative to the baseline. This improvement indicates that the applied geometric modification promotes more effective static pressure rise within the diffuser passage, consistent with the flow features observed in Fig. 14. In contrast, Case9 shows a negative pressure recovery coefficient, indicating a local pressure deficit within the passages. This behavior suggests the presence of strong adverse flow phenomena, including flow separation, which can be attributed to the specific leading edge geometry and suction side curvature, as also evidenced in Fig. 14. A similar trend is observed for the total pressure loss coefficient in Fig. 16(b). While most modified configurations achieve a reduction in loss relative to the baseline, Case7 and Case9 show performance deterioration. This degradation is likely associated with enhanced boundary layer thickness and increased secondary flow activity within the diffuser passages. Overall, these results highlight the trade-off between pressure recovery and loss generation in diffuser design. Furthermore, they demonstrate that the application of the modal shape modification technique to the diffuser vane surface can effectively improve the diffuser aerodynamic performance.

5.4. Effects of diffuser vane configuration on flow characteristics within the diffuser passages near-stall

Due to the nature of diffuser, boundary layer separation tends to generate along the vane surfaces within the diffuser passages of centrifugal compressors. This phenomenon leads to increased flow unsteadiness and enhanced turbulence levels in the affected region. Turbulent kinetic energy (TKE) is an important indicator for quantifying the intensity of turbulent fluctuations within the flow field. As separation develops, flow deceleration and the formation of turbulent eddies contribute to a rise in TKE. Fig. 17 shows the distribution of TKE on the mid-span plane inside the diffuser passages for the reference and different designed configurations under near-stall condition ($\phi = 0.88$). Note that Case9 represents the last stable operating point on the compressor map. The TKE values are normalized by the impeller tip velocity. The high-magnitude TKE regions, highlighted in red in Fig. 17, originate from flow separation near the vane surfaces and extend downstream as the passage expands. A noticeable reduction in high-TKE regions is observed for Case5 (maximum stall margin) and Case11 (maximum efficiency) compared with the reference diffuser. This improvement can be attributed to modifications in the vane geometry, particularly near the leading edge, which promote controlled mixing between the high-energy mainstream flow and low-energy near-wall fluid. This mixing mitigates adverse pressure gradients and delays the onset of flow separation, allowing the flow to remain attached over a longer portion of the vane surface. However, the effectiveness of these geometric modifications is limited in Case9. In this configuration, large-scale separation persists and occupies a significant portion of the diffuser passage, resulting in elevated TKE levels. This behavior highlights the strong dependence of separation characteristics on the specific vane geometry and indicates that not all design variations are equally effective in suppressing turbulent losses.

Fig. 18(a) presents a comparison of the pressure distribution (blade loading) along the mid-span of the diffuser vane for the baseline and various designed cases under near-stall conditions, corresponding to Fig. 17. The x-axis shows the normalized streamwise direction, while the y-axis represents the normalized static pressure. For Case5 and Case11, the blade loading profiles shows a clear improvement relative to the reference configuration on both the pressure and suction sides, while main-

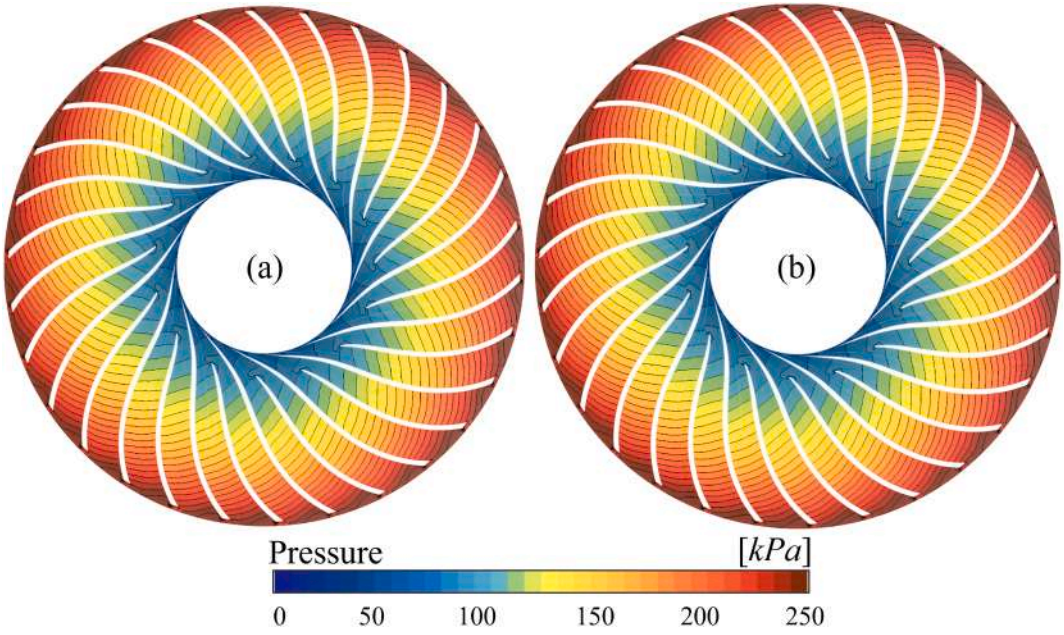


Fig. 13. Comparison of pressure distributions on the mid-span plane inside the impeller passages: (a) Case5, (b) Case9.

taining a similar overall distribution shape. In contrast, Case9 exhibits a noticeable modification in the blade loading profile compared with other designs, accompanied by a substantial reduction in pressure magnitude, particularly in the downstream region. At this off-design condition, the operating mass flow rate is relatively low compared with that of Case9, which operates closer to its stability limit. As highlighted by the red dashed circle in the figure, Case9 shows a pronounced pressure drop in the normalized streamwise range of 0.2 - 0.4. This behavior is attributed to increased flow blockage and the development of a shock structure as the operating condition approaches the surge limit.

Fig. 18(b) shows the circumferentially mass-flow-averaged entropy production ($\Delta S_{production}$) along the diffuser passage from inlet to outlet under near-stall operating conditions for the reference and designed cases. In all configurations, $\Delta S_{production}$ increases progressively in the streamwise direction, which can be attributed to the onset and subsequent growth of boundary layer separation within the passage. Case5 and Case11 exhibit lower entropy production levels than the baseline configuration, which is consistent with the performance trends reported in Fig. 17. In contrast, Case9 produces the highest entropy magnitude, particularly downstream of the normalized streamwise location of approximately 0.4. This indicates the presence of a fully developed separated flow region in the passage, in agreement with the flow features illustrated in Fig. 18(a).

5.5. Optimal diffuser vane configuration

The CFD data obtained from fourteen design cases, generated by the DOE approach, were employed to construct a surrogate model based on the GA algorithm. As described in Section 4.4, a MOGA approach was then applied to determine the optimal combination of mode number and amplitude that simultaneously maximizes isentropic efficiency at the design operating point and improves compressor stall margin. The resulting Pareto distribution is presented in Fig. 19, illustrating the trade-off between compressor efficiency and stall margin improvement. The non-dominated optimal solutions defining the Pareto front are indicated by black solid circles. As can be observed, improvements in stall margin are generally achieved with only marginal variations in aerodynamic efficiency along the Pareto front. For centrifugal compressors equipped with vaned diffusers, stall margin enhancement is particularly important due to its direct impact on operational stability and safe operating range. Therefore, the present optimization mainly emphasizes maximizing stall margin while maintaining efficiency within an acceptable level. Since the design objective is explicitly prioritized according to the operational requirements of the compressor, the selection process is deterministic and fully traceable. The chosen optimal solution therefore corresponds to the Pareto-optimal design that achieves the largest improvement in stall margin without introducing a significant penalty in aerodynamic efficiency. This selected optimal design is highlighted by the red circle in Fig. 19. The corresponding optimized design variables and objective function values predicted by the MOGA, are summarized in Table 4. For validation, the isentropic efficiency and stall margin associated with the optimal configuration were also evaluated using CFD simulations. The comparison indicates that the deviations between the MOGA predictions and the RANS results are 0.18% for isentropic efficiency and 0.14% for stall margin, respectively. These relatively small discrepancies confirm the robustness and predictive capability of the proposed CFD-based optimization framework for identifying improved diffuser vane configurations under the considered operating conditions.

Table 4
Optimal design variables and objective functions.

Design variables		Objective functions			
Mode number (n)	Amplitude (A/d)	MOGA		CFD	
		η	ΔSM	η	ΔSM
11	-0.811	86.29	2.726	86.45	2.722

Fig. 20 compares the aerodynamic performance maps of the compressor for the baseline and optimized diffuser vane configurations. The results indicate that the total pressure ratio remains nearly unchanged near the choke condition and at the design operating point. However, as the compressor operating point approaches the surge limit, the optimal configuration exhibits a noticeable increase in total pressure ratio. In contrast, the isentropic efficiency exhibits a consistent improvement across the entire operating range, from choke to surge, when the optimized diffuser vane is employed. This enhancement suggests more effective flow guidance and reduced aerodynamic losses within the diffuser passage. Moreover, as shown in Fig. 20, the minimum achievable mass flow rate is reduced for the optimal configuration, indicating an

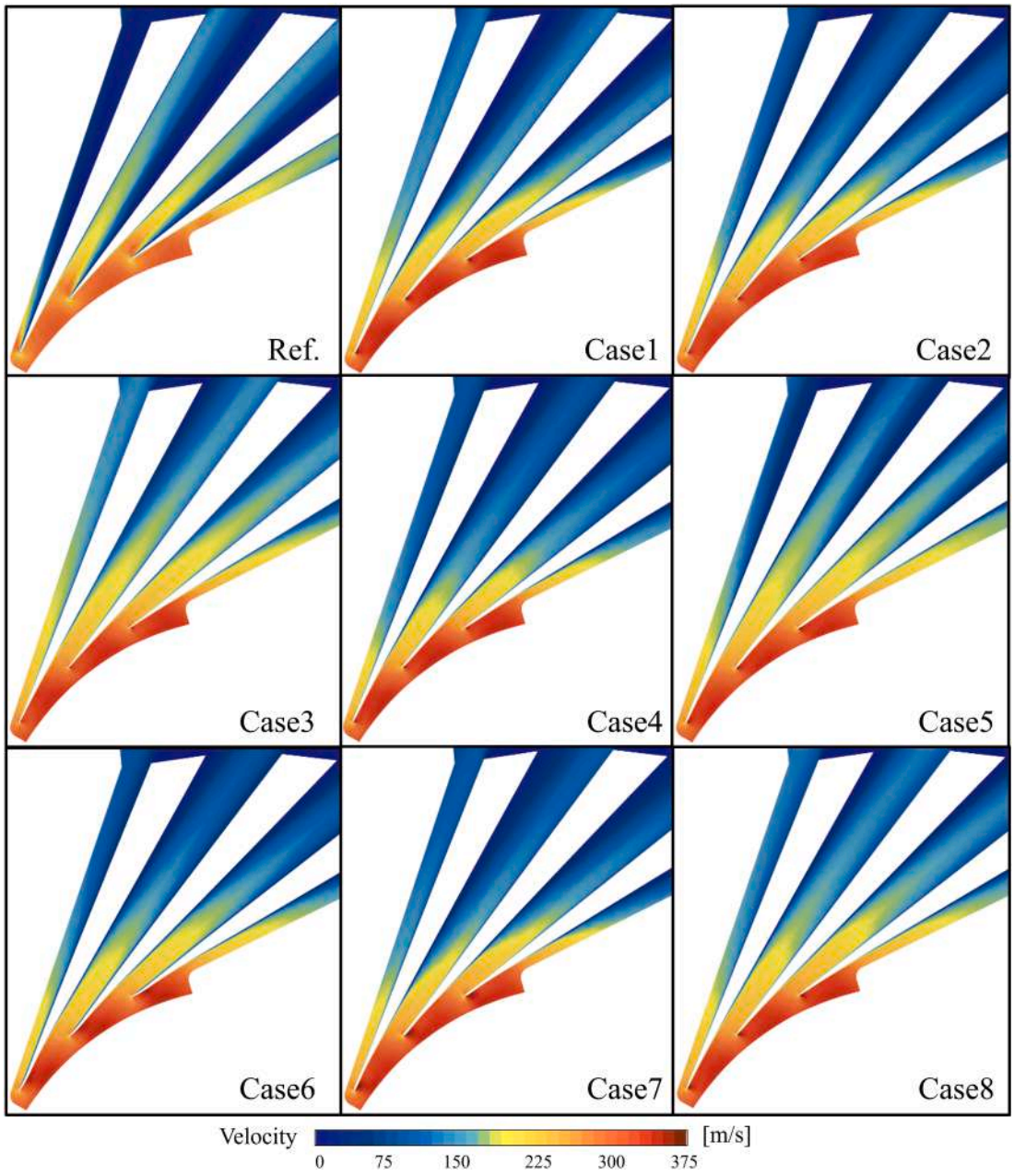


Fig. 14. Velocity contours on the mid-span plane of the diffuser passages for the baseline and all designed cases (Part 1), (Part 2).

extension of the stable operating range. Overall, this leads to a 2.722% increase in stall margin compared with the baseline case, highlighting the beneficial impact of the diffuser vane optimization on compressor stability.

Fig. 21 presents the velocity field distributions calculated by the RANS approach for the optimized vane configuration at the design operating point. The contours are shown on spanwise planes located at 10%, 50%, and 90% of the vane height within the diffuser passage. As the cutting plane moves from the hub toward the shroud, the velocity magnitude at the diffuser throat increases, and the high-velocity core shifts toward the main passage. At 10% span, near the hub, a separated boundary layer is evident on the pressure side of the diffuser vane. At mid-span (50%) and near the shroud (90%), this low-momentum region becomes weaker and is convected further downstream toward the trailing edge. A comparison between the mid-span results of the optimized vane configuration in Fig. 21 and the baseline case (Fig. 14) indicates a clear reduction in the low-momentum flow region along the suction side. This improvement is attributed to the modified diffuser geometry, which suppresses flow separation and delays its onset further downstream.

To assess the effect of the optimal diffuser vane geometry on the internal flow structure under off-design conditions, mid-span velocity contours at a normalized mass flow rate of $\phi = 0.88$ are compared between the baseline and optimized cases in Fig. 22(a) and (b), respectively. The optimized vane clearly shows a higher velocity magnitude at the diffuser throat relative to the baseline design. Moreover, the large separated flow region observed in the baseline configuration, indicated by the dark blue zone within the diffuser passage, is effectively eliminated in the optimized configuration. The suppression of flow separation leads to improved compressor efficiency and an extended stable operating range. At a lower mass flow rate of $\phi = 0.85$, the baseline configuration fails to maintain a stable operating condition, as evidenced by the compressor performance map in Fig. 18. In contrast, the optimized vane configuration continues to operate stably. The corresponding mid-span velocity distribution for the optimized cases is shown in Fig. 22(c).

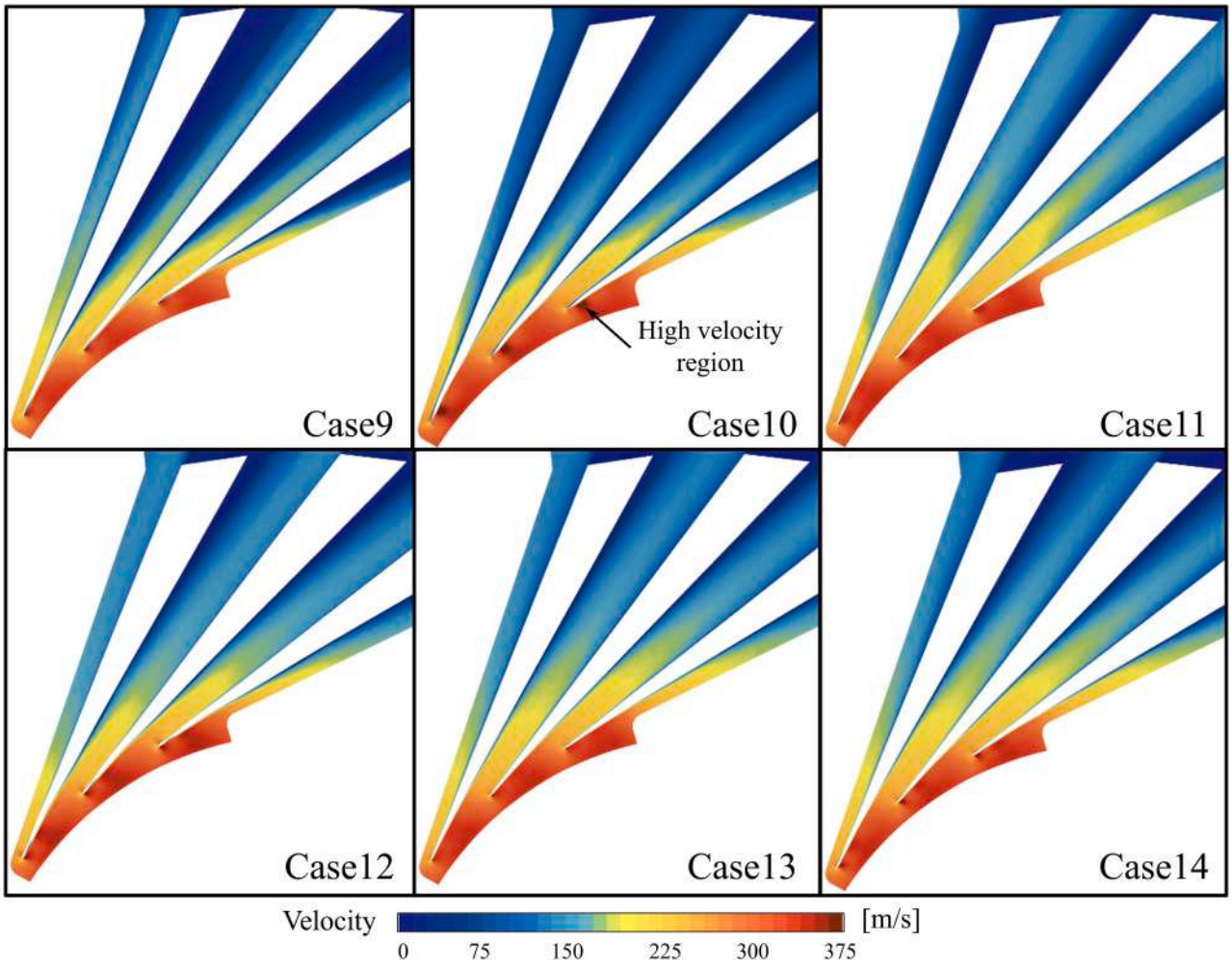


Fig. 14. Continue.

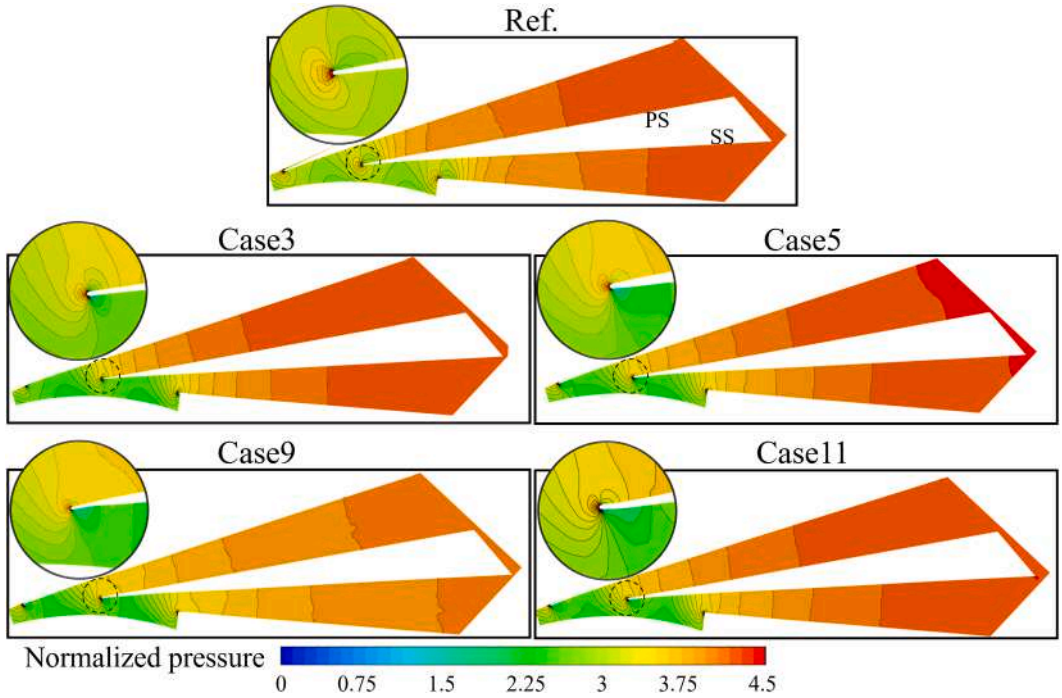


Fig. 15. Comparison of normalized static pressure distributions at the mid-span plane inside the diffuser passages for the reference and four designed configurations.

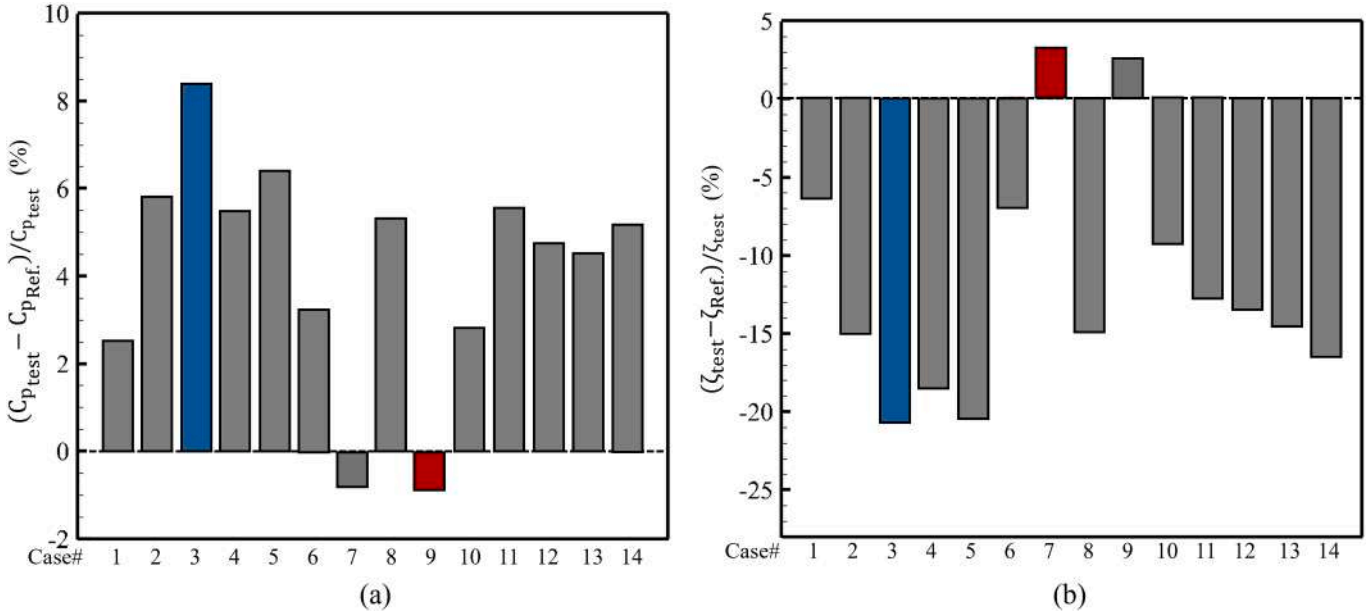


Fig. 16. Comparison of the influence of diffuser surface geometric modifications on aerodynamic performance: (a) pressure recovery coefficient, (b) total pressure loss coefficient.

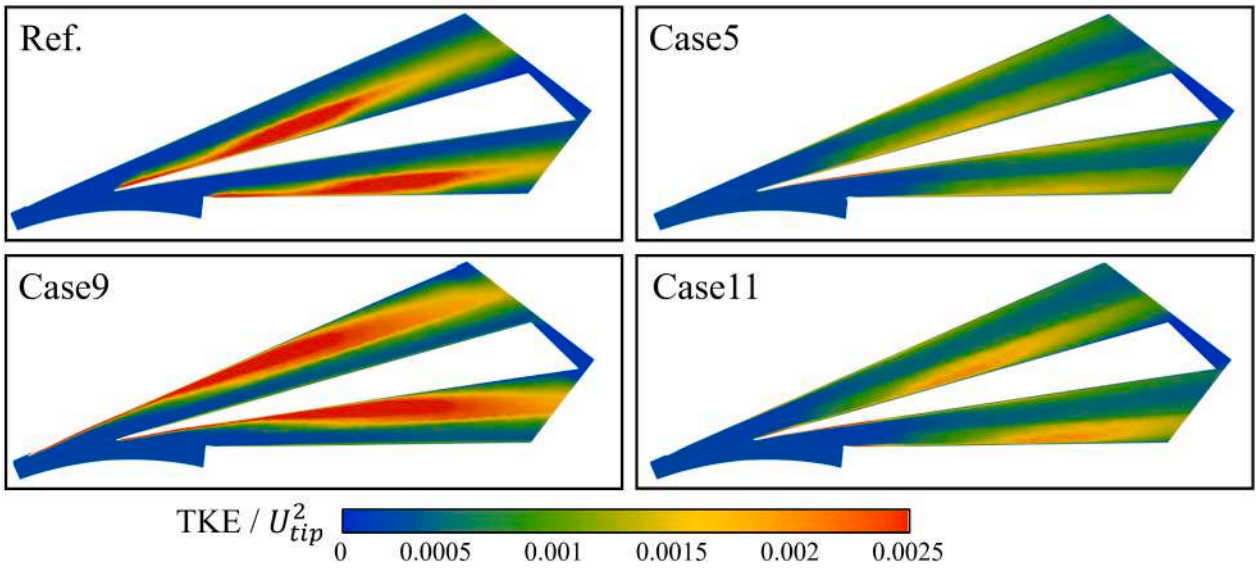


Fig. 17. Turbulence kinetic energy distribution on the mid-span plane inside the diffuser passage for various cases under near-stall condition ($\phi = 0.88$).

Although the overall velocity level within the passage decreases compared to the $\phi = 0.88$ condition, the flow remains well attached inside the passage, with no significant separation observed. It is also noteworthy that, at $\phi = 0.85$, the velocity magnitude near the diffuser throat increases relative to the $\phi = 0.88$ condition. This trend is attributed to the development of a shock wave at the impeller/diffuser interface as the mass flow rate is further reduced.

Fig. 23 presents the normalized static pressure distributions along the suction and pressure sides of the diffuser vane for both the baseline and optimized configurations under near-stall conditions ($\phi = 0.88$). In the optimized design, a general increase in pressure magnitude is observed on both sides of the diffuser vane compared with the baseline case. As shown in Fig. 23, the reference configuration exhibits a pronounced low-pressure region near the leading edge on the suction side. This feature is associated with flow separation within the diffuser passage, which promotes the formation of a separated flow zone close to the leading edge. As a result, the effective flow area at the diffuser throat is reduced, increasing blockage and ultimately triggering the onset of diffuser rotating stall. Similar flow behavior has been reported in previous studies [32,51]. In contrast, the optimal case does not show this low-pressure region on the suction surface, indicating a suppression of leading edge separation. Furthermore, although a low-pressure region is still present on the pressure side in both configurations, its magnitude is noticeably reduced in the optimized cases, and the associated separated region is considerably smaller. Overall, these modifications suggest a more stable flow structure and improved aerodynamic performance under near-stall conditions.

To examine the evolution of flow separation inside the diffuser passage, contours of entropy production at several streamwise locations are presented for near-stall operation ($\phi = 0.88$) for both the baseline and optimal configurations (Fig. 24(a) and (b), respectively). The optimized case exhibits a consistent reduction in entropy production across

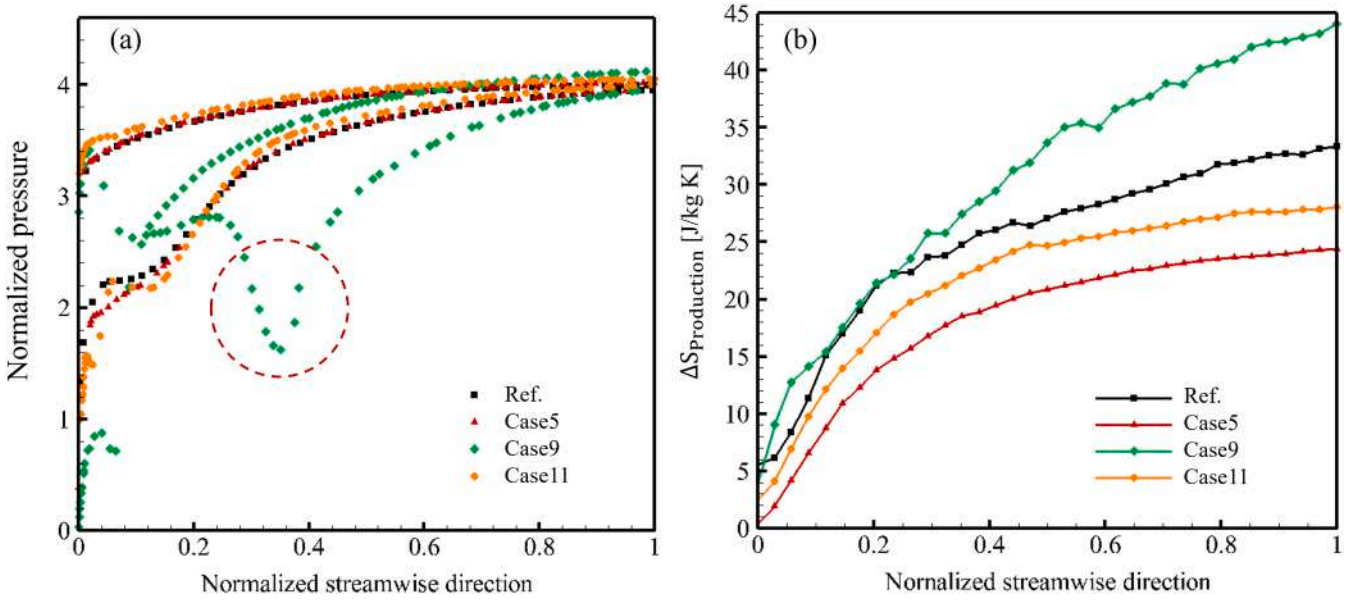


Fig. 18. (a) Blade loading profiles for various diffuser vane configurations at mid-span under near-stall condition ($\phi = 0.88$), (b) circumferentially mass flow-averaged entropy production from the diffuser inlet to outlet under near-stall condition ($\phi = 0.88$).

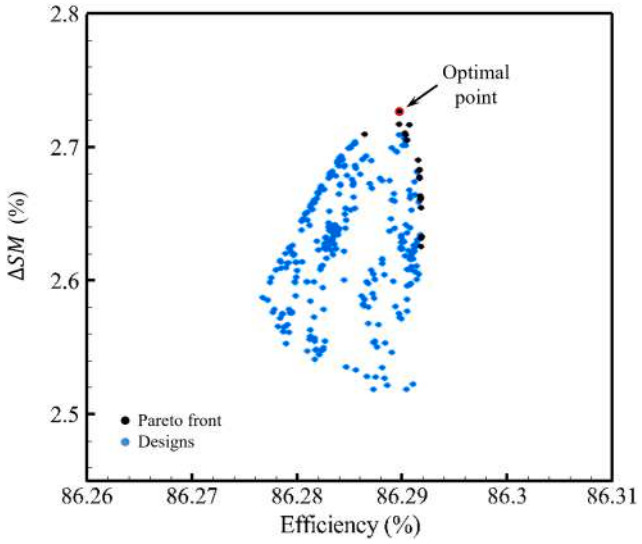


Fig. 19. Pareto front and optimal point.

all surfaces compared with the reference design. In the baseline configuration, a region of high-magnitude entropy develops along the suction side surface and progressively extends toward the trailing edge, indicating the presence and growth of flow separation within the diffuser passage. However, this high-entropy region is noticeably reduced in the optimized geometry. This behavior indicates that the modified vane design effectively suppresses flow separation, promotes reattachment, and enhances pressure recovery along the diffuser surfaces.

To further evaluate the influence of the diffuser vane geometry on the three-dimensional separated flow within the diffuser passage, Fig. 25 presents a comparison of the Q_{cr} isosurfaces for the baseline and optimized diffuser configurations. For consistency, a constant Q_{cr} value of 20,000 s^{-2} was used to generate the isosurfaces for both cases. As shown in Fig. 25(a), distinct flow separation structures develop within the diffuser passage of the baseline configuration, particularly near the pressure side of the diffuser vane, indicating the presence of strong vortical flow associated with boundary layer separation. In contrast, the optimized diffuser shown in Fig. 25(b) exhibits a significant reduction in these separation structures. The suppression of the separated flow results in a more attached and spatially uniform flow field throughout the diffuser passage, demonstrating the effectiveness of the optimized vane geometry in improving the internal flow characteristics and reducing flow separation.

The pressure distribution at the diffuser throat plays a key role in governing flow separation and blockage inside the diffuser passage [50,51]. To assess the effect of the modified diffuser vane on this behavior, the circumferential distribution of normalized pressure at the diffuser throat, 90% span, under near-stall conditions ($\phi = 0.88$) is shown in Fig. 26 for both the reference and optimized configurations. For clarity of the flow features, the single-passage computational results have been circumferentially duplicated and rotated to enhance visualization of the flow structures. Compared with the baseline case, the optimized configuration exhibits a wider range between minimum and maximum pressure levels, accompanied by a smoother circumferential variation. This trend indicates a more gradual pressure recovery and improved flow uniformity at the diffuser inlet. These characteristics are consistent with local flow deceleration and a more favorable incidence angle at the diffuser vanes, which together help delay flow separation and ultimately contribute to an increased stall margin.

It has been reported that the stall margin of centrifugal compressors can be improved by increasing the radial velocity component [52]. Fig. 27(a) and (b) show the spanwise distributions of radial and tangential velocity components at the diffuser inlet, near the vane leading edge, under near-stall conditions ($\phi = 0.88$) for both the reference and optimized configurations. The results indicate that the geometric modification of the diffuser vane significantly alters the diffuser inlet flow structure. As shown in Fig. 27(a), the optimal case exhibits a more uniform radial velocity profile compared to the baseline case. In addition, the magnitude of negative radial velocity near the shroud, associated with local reversed flow, is noticeably reduced. The location of zero radial velocity is also shifted toward a higher span position, moving from approximately 0.93 in the reference case to about 0.98 in the optimized one. This modification leads to a reduction of flow disturbances inside the diffuser passage, which contributes to an extension of the stable operating range. Furthermore, Fig. 27(b) shows that the tangential velocity distribution becomes more uniform along the spanwise direction in the optimized case, while its overall magnitude increases along the span. This helps maintain flow attachment near the shroud and suppresses the development of localized reverse flow.

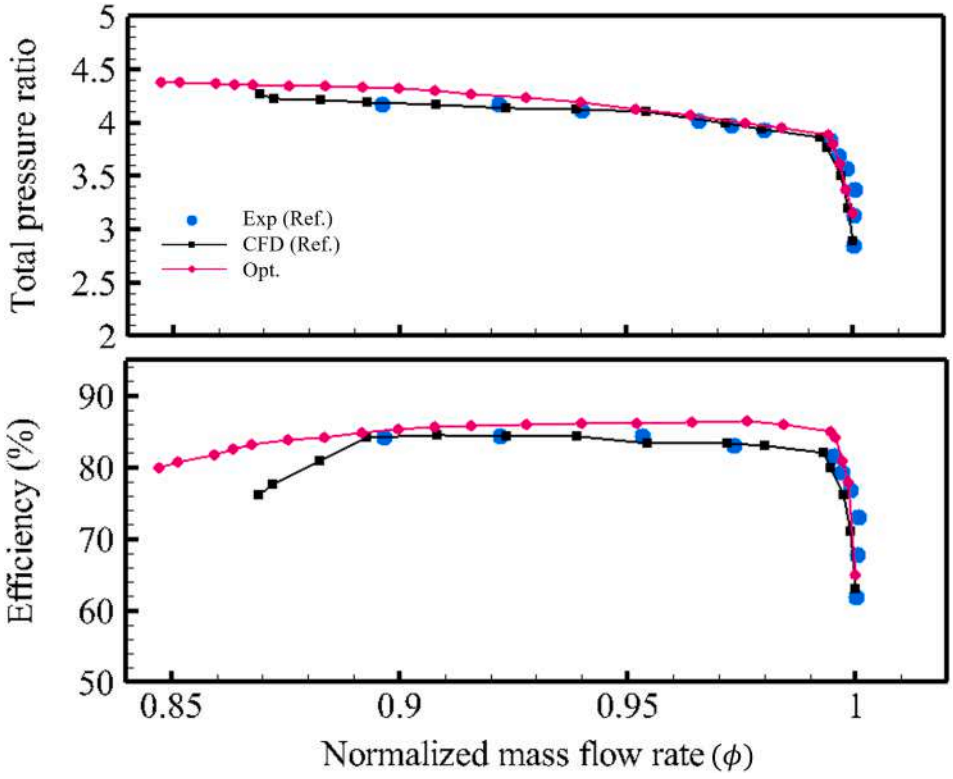


Fig. 20. Compressor performance map for the baseline and optimal diffuser vane configurations.

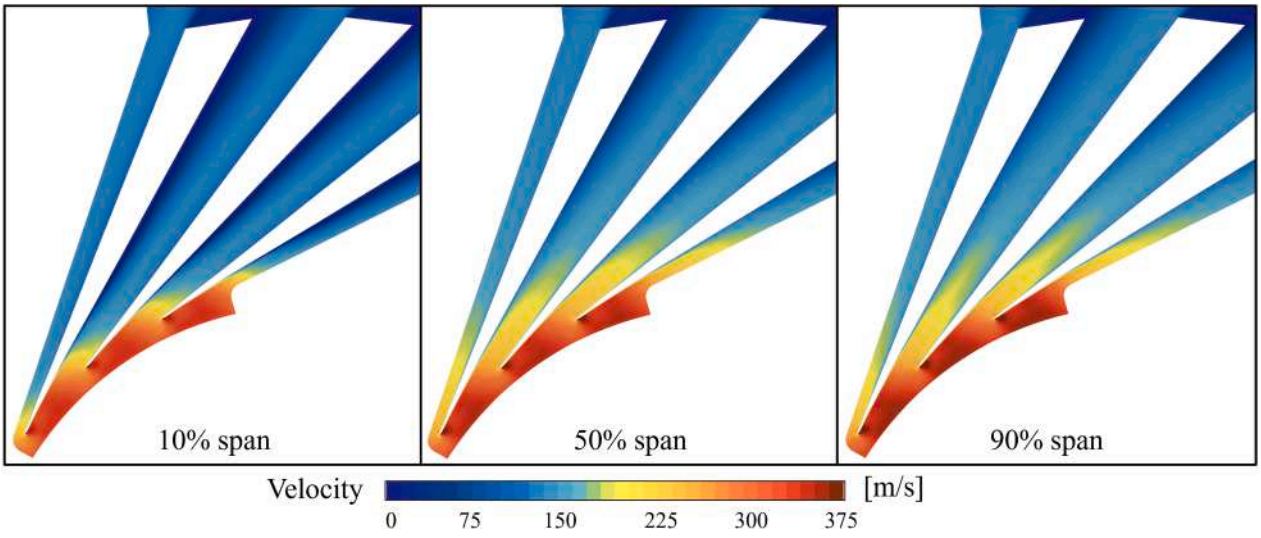


Fig. 21. Velocity contour on various spanwise cutting planes within the optimized diffuser vane passage at the design operating condition.

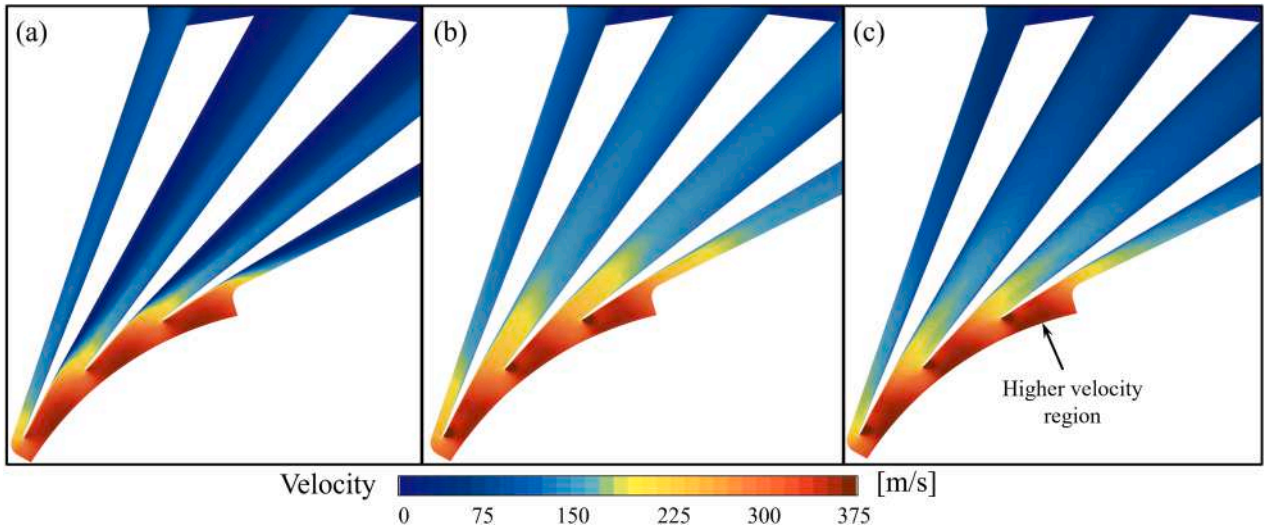


Fig. 22. Velocity contours on the mid-span plane: (a) baseline case at $\phi = 0.88$, (b) optimized case at $\phi = 0.88$, (c) optimized case at $\phi = 0.85$.

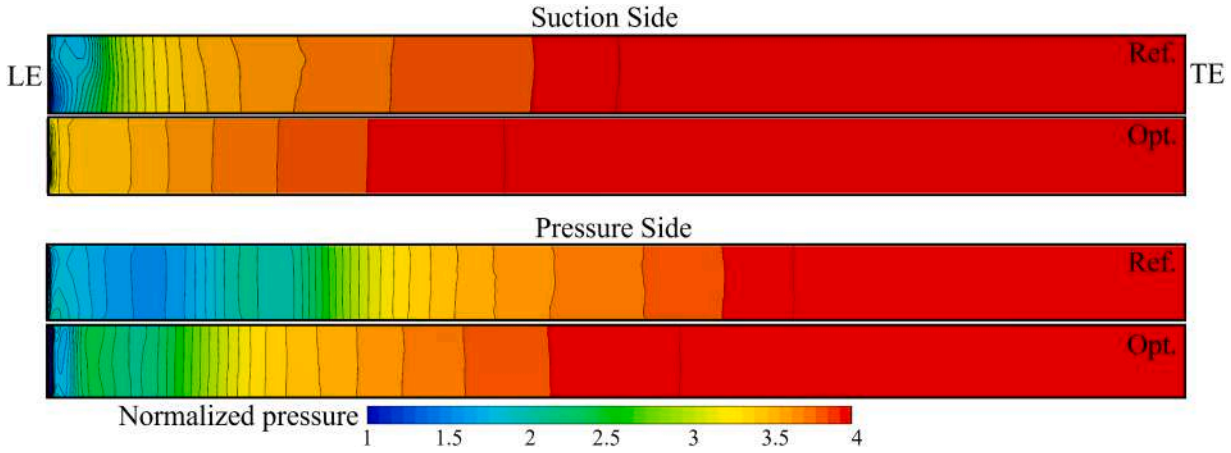


Fig. 23. Normalized static pressure distribution along the suction and pressure surfaces of the diffuser vane for the baseline and optimal configurations under near-stall condition ($\phi = 0.88$).

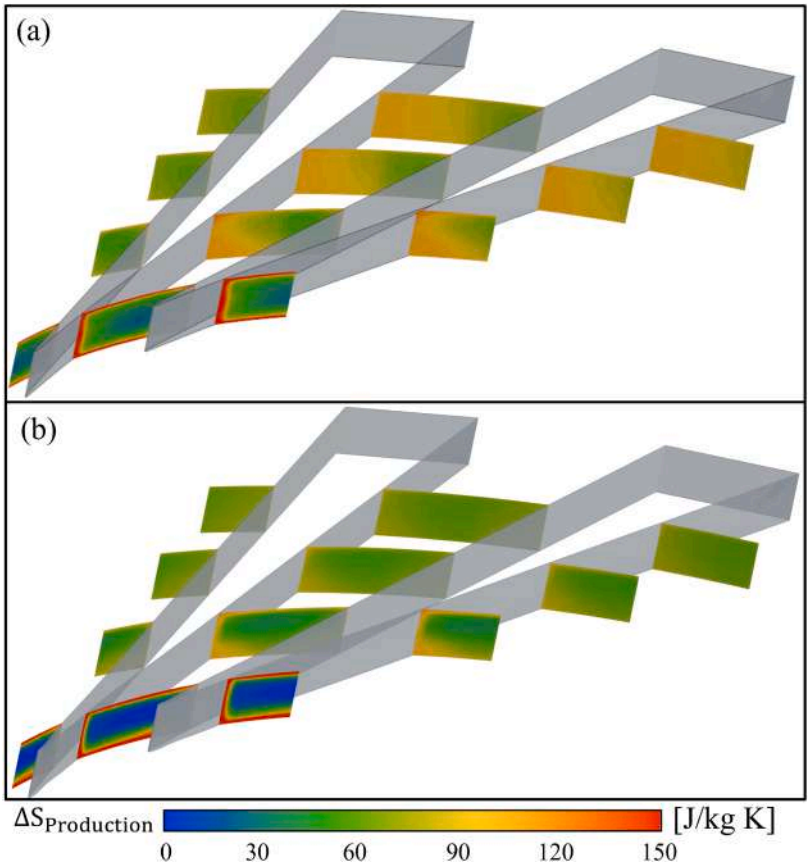


Fig. 24. Entropy production distributions on several streamwise planes along the diffuser passage under near-stall condition ($\phi = 0.88$): (a) baseline configuration, (b) optimized configuration.

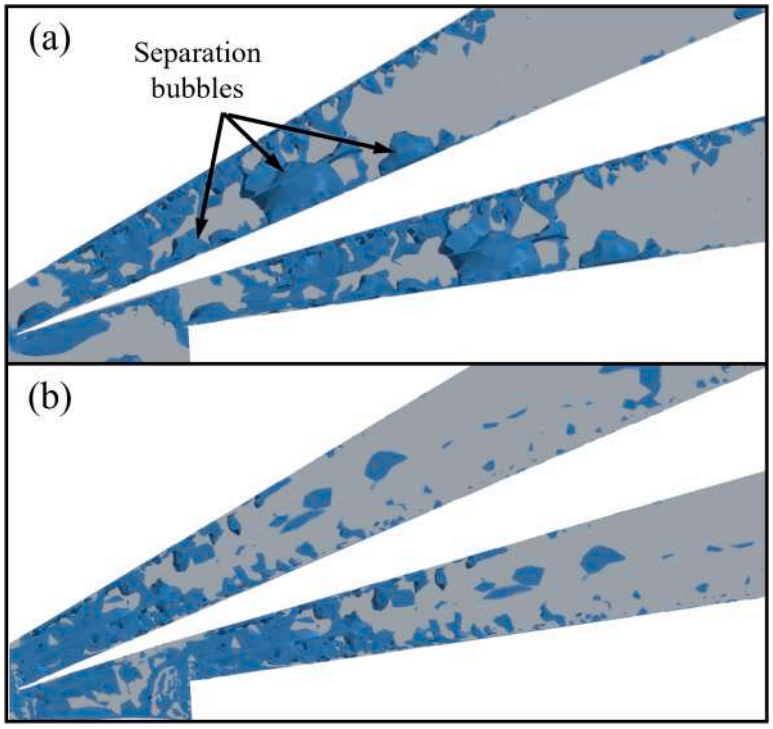


Fig. 25. Iso-surfaces of Q_{cr} ($=20{,}000\ s^{-2}$) within the diffuser passage: (a) reference case, (b) optimized case.

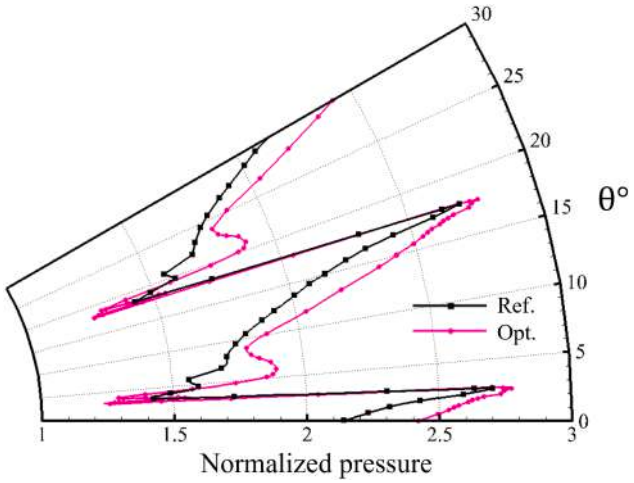


Fig. 26. Pressure distribution at near-stall condition ($\phi = 0.88$) at 90% span along the circumferential direction for the baseline and optimized configurations.

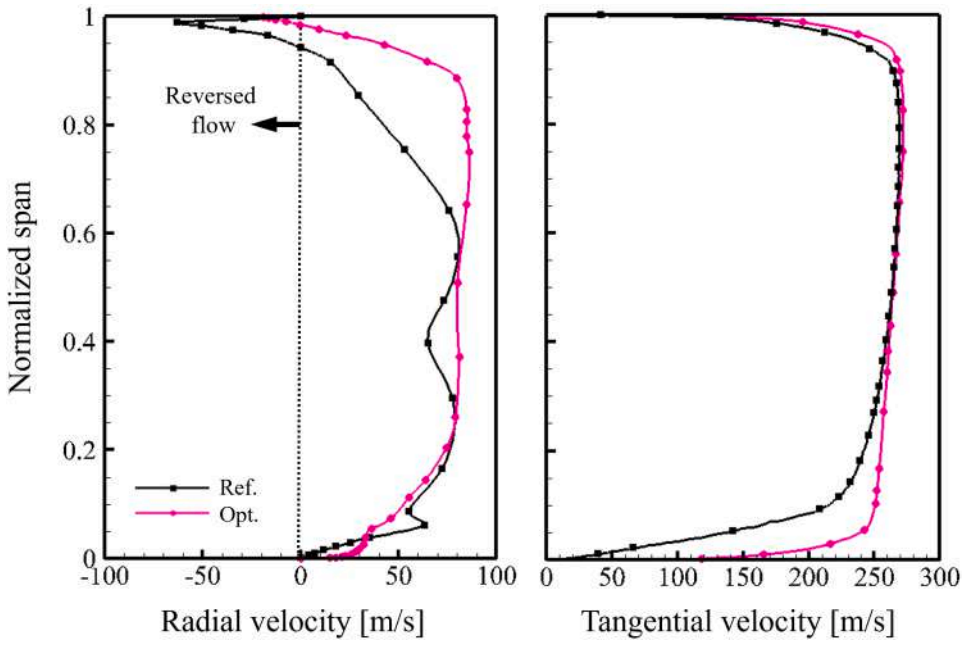


Fig. 27. Comparison of spanwise velocity profiles at the diffuser throat near the vane leading edge ($\phi = 0.88$) for the baseline and optimized configurations: (a) radial velocity component, (b) tangential velocity component.

6. Conclusions

In this work, the diffuser vane of a transonic centrifugal compressor was optimized using a modal shape parametrization approach applied to the vane surface. The mode number and amplitude were selected as design variables, and a GA surrogate model was constructed from a CFD database. A MOGA algorithm was then utilized to identify an optimal diffuser vane configuration that improves both aerodynamic efficiency and stall margin.

1. The results indicated that modification to the diffuser surface geometry had a pronounced impact on compressor performance and operating range, while the upstream impeller flow remains largely unaffected. Among the candidate designs, Case3 achieved the highest pressure ratio increase at the design point, reaching approximately 11% relative to the reference case. Case11 demonstrated the best efficiency (3.1% improvement), whereas Case5 showed the greatest enhancement in stall margin (2.52%).

2. For the modified geometries, the extent of flow separation within the diffuser passage was generally reduced, although its spatial distribution varied depending on the vane shape. Configurations with negative amplitudes with respect to the camber line tended to show improved stall margin. This behavior is linked to changes in the leading edge geometry introduced by the modal shape parameterization, which in turn reduces the incidence angle. Consequently, the stagnation pressure distribution near the diffuser throat is altered, affecting boundary layer development and delaying flow separation on the vane surfaces.

3. The analysis of pressure recovery and total pressure loss coefficients indicated that most of designed cases outperform the baseline configuration. In particular, Case3 showed the most significant enhancement relative to the reference case with approximately a 9% increase in pressure recovery. Furthermore, TKE distributions at off-design conditions revealed a reduction in high-TKE regions for the modified designs, indicating weaker flow separation. This improvement is attributed to enhanced momentum exchanged between the high-speed core flow and the low-energy near-wall region induced by the modified geometry.

4. The optimized diffuser vane configuration consistently improved isentropic efficiency across the entire operating range, with an increase of approximately 4.1% at the design point. In addition, the stall margin

was extended by about 2.72%, which is attributed to favorable modifications of the velocity field near the diffuser throat that delays separation onset and its downstream propagation.

5. Under near-stall conditions, the optimized design produced a wider circumferential pressure variation at the diffuser throat near the vane leading edge. This contributes to a smoother pressure recovery and improves inlet flow uniformity. Moreover, the optimal vane geometry demonstrated a more uniform radial velocity distribution near the leading edge, while the magnitude of reverse flow near the shroud is reduced. An increase in the tangential velocity component along the spanwise direction further promotes flow attachment near the shroud, thereby suppressing local flow reversal.

This work demonstrates the effectiveness of a modal shape parametrization technique applied to diffuser vane optimization in enhancing compressor stability within a RANS-based framework. Building on these findings, future research should focus on detailed flow-physics investigation using high-fidelity, time-resolved simulations. Such unsteady analyzes would provide deeper insight into the mechanisms governing rotating stall inception and transient flow dynamics inside diffuser channels.

CRediT authorship contribution statement

Ali Zamiri: Writing – review & editing, Writing – original draft, Validation, Software, Methodology, Investigation, Conceptualization; **Sam Lovett:** Methodology; **Thomas C.S. Rendall:** Writing – review & editing, Methodology; **Minsuk Choi:** Writing – review & editing; **Giovanna Barigozzi:** Writing – review & editing.

Declaration of competing interest

The authors declare that they have no known competing financial interests or personal relationships that could have appeared to influence the work reported in this paper.

Data availability

No data was used for the research described in the article.

References

[1] D. Japikse, A critical evaluation of three centrifugal compressors with pedigree data sets: part 5–studies in component performance, J. Turbomach. 109 (1) (1987) 1–9. https://doi.org/10.1115/1.3262064

[2] K.H. Lüdtke, Process Centrifugal Compressors: Basics, Function, Operation, Applications, 1st ed., Springer-Verlag New York, 2004. https://doi.org/10.1007/978-3-662-09449-5

[3] J.A. Hoffmann, Effects of free-stream turbulence on diffuser performance, ASME J. Fluids Eng. 103 (1981) 385–390. https://doi.org/10.1115/1.3240795

[4] A. Zamiri, B.J. Lee, J.T. Chung, Numerical evaluation of transient flow characteristics in a transonic centrifugal compressor with vaned diffuser, Aerosp. Sci. Technol. 70 (2017) 244–256. https://doi.org/10.1016/j.ast.2017.08.003

[5] L. Yan, L. Yuchen, H. Hao, X. Jun, Multifractal analysis of flow instability of centrifugal compressor with dynamic pressure, Alex. Eng. J. 72 (2023) 181–193. https://doi.org/10.1016/j.aej.2023.03.069

[6] Y. Zhang, X. Lu, Y. Zhang, Z. Zhang, X. Dong, G. Han, Stall behavior in an ultrahigh-pressure-ratio centrifugal compressor: backward-traveling rotating stall, J. Turbomach. 144 (10) (2022) 101010. https://doi.org/10.1115/1.4050918

[7] P. Aref, M. Ghoreyshi, A. Jirasek, M. Satchell, CFD validation and flow control of RAE-M2129 S-duct diffuser using CREATE-AV Kestrel simulation tools, Aerosp. J. 5 (1) (2018) 31. https://doi.org/10.3390/aerospace5010031

[8] M. Zhang, C. Hu, X. Xu, J. Du, J. Zhang, Adaptive jet flow control for performance improvement via coupling stator-blade with rotor-tip injections in a transonic compressor, Phys. Fluids 36 (2024) 116144. https://doi.org/10.1063/5.0238055

[9] S.E. Ak, S. Cadirici, Investigation of suction flow control on centrifugal compressor with vaned diffuser, Energies 15 (2) (2024) 583. https://doi.org/10.3390/en15020583

[10] G.J. Skoch, Experimental investigation of centrifugal compressor stabilization techniques, J. Turbomach. 125 (4) (2003) 704–713. https://doi.org/10.1115/1.1624846

[11] Q. Liu, X. Chen, X. Song, Investigating the effects of streamwise riblets on flow separation in low-Reynolds-number compressor cascades using direct numerical simulation, Aerosp. Sci. Technol. 173 (2026) 111800. https://doi.org/10.1016/j.ast.2026.111800

[12] Y. Zhao, X. Li, Z. Liu, M. Zhao, S. Gao, X. Li, Unsteady mechanisms of flow stability improvement for a compressor with self-circulating casing treatment, Phys. Fluids 37 (2025) 067102. https://doi.org/10.1063/5.0260713

[13] R.A. Adjei, C. Fan, S. Ijaz, H. Zou, Aerodynamic optimization for stability improvement of a centrifugal compressor using arbitrary-shape volute design, Case Stud. Therm. Eng. 73 (2025) 106654. https://doi.org/10.1016/j.csite.2025.106654

[14] A. Zamiri, M. Choi, J.T. Chung, Effect of blade squealer tips on aerodynamic performance and stall margin in a transonic centrifugal compressor with vaned diffuser, Aerosp. Sci. Technol. 123 (2022) 107504. https://doi.org/10.1016/j.ast.2022.107504

[15] F. Ashrafi, H.D. Vo, Passive flow control at impeller radial bend for stall delay in centrifugal compressors with fishtail pipe diffusers, Aerosp. Sci. Technol. 145 (2024) 108840. https://doi.org/10.1016/j.ast.2023.108840

[16] W. Zhao, Z. Li, Z. Qu, J. Zhao, Q. Li, Investigation of flow mechanisms and performance in a centrifugal compressor with a novel adjustable vane height diffuser, Aerosp. Sci. Technol. 178 (2026) 112399. https://doi.org/10.1016/j.ast.2026.112399

[17] A. Zamiri, K.S. Park, M. Choi, J.T. Chung, Optimization of diffuser vane cavity in a transonic centrifugal compressor for improved aerodynamic efficiency and operating stability, Eur. J. Mech. B Fluids 114 (2025) 204338. https://doi.org/10.1016/j.euromechflu.2025.204338

[18] Q. Cui, G. Qin, C. Jia, Y. Wang, J. Lei, Numerical investigation of centrifugal compressor stability enhancement using vaned diffuser endwall contouring technology, Energy Sci. Eng. 10 (2022) 2808–2826. https://doi.org/10.1002/ese3.1169

[19] A. Zamiri, B.J. Lee, J.T. Chung, Influence of the inclined leading edge diffuser vanes on the aerodynamic performance of a transonic centrifugal compressor, J. Mech. Sci. Technol. 31 (11) (2017) 5557–5568. https://doi.org/10.1007/s12206-017-1050-z

[20] A. Zamiri, K.S. Park, M. Choi, J.T. Chung, Transient analysis of flow unsteadiness and noise characteristics in a centrifugal compressor with a novel vaned diffuser, Appl. Sci. 11 (2021) 3191. https://doi.org/10.3390/app11073191

[21] G. Han, C. Yang, S. Wu, S. Zhao, X. Lu, The investigation of mechanisms on pipe diffuser leading edge vortex generation and development in centrifugal compressor, Appl. Therm. Eng. 219 (2023) 119606. https://doi.org/10.1016/j.applthermaleng.2022.119606

[22] M. Zhang, M. Qi, Effects of endwall clearances of variable diffuser vane on centrifugal compressor performance, Aerosp. Sci. Technol. 153 (2024) 109459. https://doi.org/10.1016/j.ast.2024.109459

[23] H. Ziatabar, M.T. Rahni, A.S. Taleghani, Aerodynamic design of a trailing-edge morphing wing using morphing function idea and meta-model optimization based on CFD approach, Int. J. Aeronaut. Space Sci. 27 (2026) 2615–2653. https://doi.org/10.1007/s42405-025-01108-0

[24] S. Abolahipour, M. Moomivand, A. Shams Taleghani, Effect of crossflow jet injection on induced aerodynamic loads between tandem surfaces in supersonic flow using SBES, Aerosp. Sci. Technol. 174 (2026) 111921. https://doi.org/10.1016/j.ast.2026.111921

[25] S. Abolahipour, Review on flow separation control: effects of excitation frequency and momentum coefficient, Front. Mech. Eng. 10 (2018) 13806756. https://doi.org/10.3389/fmech.2024.1380675

[26] A.S. Taleghani, M. Izadi, Multiobjective optimization of a single slotted flap using artificial neural network and metaheuristic algorithms, Front. Mech. Eng. 8 (2024) 151. https://doi.org/10.1061/JENMDT.EMENG-8015

[27] G.J. Skoch, P.S. Prahst, M.P. Wernet, A.J. Strazisar, Laser Anemometer Measurements of the Flow Field in a 4:1 Pressure Ratio Centrifugal Impeller, 1997. ASME Paper No 97-GT-342, https://doi.org/10.1115/97-GT-342

[28] T.F. McKain, G.J. Holbrook, Coordinates for a High Performance 4:1 Pressure Ratio Centrifugal Compressor, Technical Report CR-204134, NASA, 1995.

[29] Siemens Digital Industries Software, Simcenter STAR-CCM+ theory guide, 2023, (Simcenter STAR-CCM+ Documentation).

[30] F.R. Menter, M. Kuntz, R. Langtry, Ten years of industrial experience with the SST turbulence model, Turbul. Heat Mass Transf. 4 (2003) 625–632.

[31] Y. Saad, Iterative Methods for Sparse Linear Systems, SIAM, Philadelphia PA USA, 2nd ed. , 2003.

[32] A. Zamiri, M. Choi, J.T. Chung, Numerical investigation of rotating stall characteristics in a full-annulus transonic centrifugal compressor, J. Propuls. Power 37 (3) (2020). https://doi.org/10.2514/1.B37891

[33] H. Chen, X. Huang, S. Fu, CFD investigation on stall mechanisms and casing treatment of a transonic compressor, in: Proc. 42nd AIAA/ASME/SAE/ASEE Joint Propuls. Conf. Exhib., Sacramento CA USA, 2006. https://doi.org/10.2514/6.2006-4799

[34] O. Dumitrescu, S. Stratila, V. Dragan, Design methods and practices for centrifugal compressor diffusers: a review, Machines 13 (11) (2025) 990. https://doi.org/10.3390/machines13110990

[35] D. Masters, N.J. Taylor, T. Rendall, C. Allen, D. Poole, Geometric comparison of aerofoil shape parameterization methods, AIAA J. 55 (5) (2017) 1575–1589. https://doi.org/10.2514/1.J054943

[36] Y. Xu, X. Gan, J. Pei, W. Wang, J. Chen, S. Yuan, Applications of artificial intelligence and computational intelligence in hydraulic optimization of centrifugal pumps: a comprehensive review, Eng. Appl. Comput. Fluid Mech. 19 (1) (2025). https://doi.org/10.1080/19942060.2025.2474675

[37] D. Masters, N.J. Taylor, T.C.S. Rendall, C.B. Allen, Multilevel subdivision parameterization scheme for aerodynamic shape optimization, AIAA J. 55 (10) (2017) 3237–3250. https://doi.org/10.2514/1.J055785

[38] S. Lovett, T.C.S. Rendall, J. De Courcy, C.B. Allen, D.J. Poole, N.J. Taylor, J. Fincham, M. Wood, N. Leppard, Modal analysis of subdivision surfaces for aerodynamic shape parameterisation, in: AIAA AVIATION Forum and ASCEND, 2025. https://doi.org/10.2514/6.2025-3622

[39] A. Zamiri, S. Lovett, D.J. Poole, T.C.S. Rendall, C.B. Allen, G. Barigozzi, J.T. Chung, Large eddy simulation in optimization of fan-shaped cooling holes using modal subdivision design variables, Int. Commun. Heat Mass Transf. 171 (2026) 110097. https://doi.org/10.1016/j.icheatmasstransfer.2025.110097
[40] E. Catmull, J. Clark, Recursively generated B-spline surfaces on arbitrary topological meshes, Comput. Aided Des. 10 (6) (1978) 350–355. https://doi.org/10.1016/0010-4485(78)90110-0
[41] C. Loop, Smooth Subdivision Surfaces Based on Triangles, Ph.D. thesis, Univ. Utah, Salt Lake City, UT, USA, 1987.
[42] M.A. Halstead, M. Kass, T. DeRose, Efficient, fair interpolation using Catmull-Clark surfaces, in: Proc. 20th Annu. Conf. Comput. Graph. Interact. Tech., 1993, pp. 35–44. https://doi.org/10.1145/166117.16612
[43] B.M. Kulfan, Universal parametric geometry representation method, J. Aircr. 45 (16) (2008) 142–158.
[44] F.J. Hickernell, A generalized discrepancy and quadrature error bound, Math. Comput. 67 (221) (1998) 299–322. https://doi.org/10.1090/S0025-5718-98-00894-1
[45] M.B. Salem, L. Tomaso, Automatic selection for general surrogate models, Struct. Multidiscip. Optim. 58 (2018) 719–734. https://doi.org/10.1007/s00158-018-1925-3
[46] M. Pournoury, D. Kim, Optimized segmented cladding fiber for extreme large mode area using latin hypercube sampling, Opt. Commun. 542 (2023) 129593. https://doi.org/10.1016/j.optcom.2023.129593
[47] K. Deb, A. Pratap, S. Agarwal, T. Meyarivan, A fast and elitist multiobjective genetic algorithm: NSGA-II, IEEE Trans. Evol. Comput. 6 (2) (2002) 182–197. https://doi.org/10.1109/4235.996017
[48] A. Zamiri, S.J. You, J.T. Chung, Large eddy simulation in the optimization of laidback fan-shaped hole geometry to enhance film-cooling performance, Int. J. Heat Mass Transf. 158 (2020) 120014.
[49] A. Zamiri, G. Barigozzi, H. Abdeh, J.T. Chung, Large eddy simulation in optimizing trench configuration to improve cooling effectiveness of a laidback fan-shaped hole, Int. Commun. Heat Mass Transf. 147 (2023) 106996. https://doi.org/10.1016/j.icheatmasstransfer.2023.106996
[50] N.A. Cumpsty, Compressor Aerodynamics, Krieger Publishing Company, Malabar FL USA, 2004.
[51] Y. Suzuki, N. Fujisawa, Y. Ohta, Unsteady pre-stall behavior in a centrifugal compressor with vaned diffuser, J. Turbomach. 146 (4) (2023) 041006. https://doi.org/10.1115/1.4064136
[52] Y. Du, H.S. Dou, F. Lu, Counter-propagating rotating stall of vaned diffuser in a centrifugal compressor near design condition, J. Turbomach. 142 (11) (2020) 111007. https://doi.org/10.1115/1.4048604